

# The prompt-afterglow connection in gamma-ray bursts: a comprehensive statistical analysis of *Swift* X-ray light curves

R. Margutti,<sup>1,2\*</sup> E. Zaninoni,<sup>2,3</sup> M. G. Bernardini,<sup>2</sup> G. Chincarini,<sup>4,2</sup> F. Pasotti,<sup>2</sup> C. Guidorzi,<sup>5</sup> L. Angelini,<sup>6</sup> D. N. Burrows,<sup>7</sup> M. Capalbi,<sup>8</sup> P. A. Evans,<sup>9</sup> N. Gehrels,<sup>6</sup> J. Kennea,<sup>7</sup> V. Mangano,<sup>10</sup> A. Moretti,<sup>2</sup> J. Nousek,<sup>7</sup> J. P. Osborne,<sup>9</sup> K. L. Page,<sup>9</sup> M. Perri,<sup>8</sup> J. Racusin,<sup>6</sup> P. Romano,<sup>10</sup> B. Sbarufatti,<sup>2,7</sup> S. Stafford<sup>11</sup> and M. Stamatikos<sup>6,11</sup>

<sup>1</sup>Harvard-Smithsonian Center for Astrophysics, 60 Garden Street, Cambridge, MA 02138, USA

<sup>2</sup>INAF Osservatorio Astronomico di Brera, via Bianchi 46, I-23807 Merate, Italy

<sup>3</sup>Physics & Astronomy Department Galileo Galilei, University of Padova, via Marzolo 8, I-35131 Padova

<sup>4</sup>Dip. Fisica G. Occhialini, Università Milano Bicocca, P.zza della Scienza 3, I-20126 Milano, Italy

<sup>5</sup>Dipartimento di Fisica, Università di Ferrara, via Saragat 1, I-44122 Ferrara, Italy

<sup>6</sup>NASA-Goddard Space Flight Center, Greenbelt, MD, USA

<sup>7</sup>Department of Astronomy & Astrophysics, 525 Davey Lab., PA, USA

<sup>8</sup>ASI Science Data Center, via G. Galilei, I-00044 Frascati, Italy

<sup>9</sup>X-ray and Observational Astronomy Group, Department of Physics & Astronomy, University of Leicester, Leicester LE1 7RH

<sup>10</sup>INAF-IASF Palermo, Via Ugo La Malfa 153, Palermo, Italy

<sup>11</sup>Department of Physics and Center for Cosmology and Astro-Particle Physics, Ohio State University, Columbus, OH 43210, USA

Accepted 2012 September 22. Received 2012 September 22; in original form 2012 March 4

## ABSTRACT

We present a comprehensive statistical analysis of *Swift* X-ray light curves of gamma-ray bursts (GRBs) collecting data from more than 650 GRBs discovered by *Swift* and other facilities. The unprecedented sample size allows us to constrain the *rest-frame* X-ray properties of GRBs from a statistical perspective, with particular reference to intrinsic time-scales and the energetics of the different light-curve phases in a common rest-frame 0.3–30 keV energy band. Temporal variability episodes are also studied and their properties constrained. Two fundamental questions drive this effort: (i) Does the X-ray emission retain any kind of ‘memory’ of the prompt  $\gamma$ -ray phase? (ii) Where is the dividing line between long and short GRB X-ray properties? We show that short GRBs decay faster, are less luminous and less energetic than long GRBs in the X-rays, but are interestingly characterized by similar intrinsic absorption. We furthermore reveal the existence of a number of statistically significant relations that link the X-ray to prompt  $\gamma$ -ray parameters in long GRBs; short GRBs are outliers of the majority of these two-parameter relations. However and more importantly, we report on the existence of a universal three-parameter scaling that links the X-ray and the  $\gamma$ -ray energy to the prompt spectral peak energy of *both* long and short GRBs:  $E_{X,\text{iso}} \propto E_{\gamma,\text{iso}}^{1.00 \pm 0.06} / E_{\text{pk}}^{0.60 \pm 0.10}$ .

**Key words:** radiation mechanism: non-thermal – gamma-ray burst: general.

## 1 INTRODUCTION

In 7 yr of operation, *Swift* (Gehrels et al. 2004) has revolutionized our understanding of the X-ray emission that follows the prompt  $\gamma$ -ray phase of gamma-ray bursts (GRBs): the X-ray afterglow. The standard afterglow theory (Meszaros & Rees 1997; Sari, Piran &

Narayan 1998) predicts that X-ray emission arises from the interaction of a relativistic outflow with the ambient medium, leading to the formation of a blast wave. In this context, short and long GRBs would naturally show similar afterglows (since the emission would be sensitive to the energy budget of the relativistic outflow but otherwise keep no memory of the origin of the outflow) *if* the properties of the environment of the two classes are also similar. This is difficult to reconcile with the massive star (long GRBs; see e.g. Woosley 1993) versus compact binary (short GRBs; see e.g.

\*E-mail: rmargutti@cfa.harvard.edu

Paczynski 1986) progenitor systems, which would instead suggest a wind density profile (i.e.  $\propto r^{-2}$ ) around long GRBs and an interstellar medium (ISM) (i.e.  $\propto r^0$ ) ambient density for short bursts. Contrary to expectations, observations are often consistent with a constant density environment (ISM) also in the case of long GRBs (e.g. Racusin et al. 2009). Moreover, the standard afterglow theory fails to explain the presence of long ( $\sim 10^4$  s) phases characterized by very mild decays (the so-called plateaus or shallow decay phases) in the X-ray light curve (LC) of many GRBs (e.g. GRB 060729; Grupe et al. 2007); it cannot account for abrupt drops of emission observed in some GRBs (e.g. GRB 070110; Troja et al. 2007, Lyons et al. 2010) and has serious difficulties explaining the X-ray flares (Chincarini et al. 2007, Falcone et al. 2007; Chincarini et al. 2010 and references therein).

As a result, a number of alternative models have been proposed. They are basically divided into two classes: accretion on to a newly born black hole which directly powers the observed X-ray LC (Kumar, Narayan & Johnson 2008) and power from a rapidly rotating magnetar (see e.g. Metzger et al. 2011 and references therein). In sharp contrast to the standard afterglow theory, these models directly relate the properties of the observed X-ray LCs to the GRB central engine.

With this work we improve our understanding of the X-ray emission of long and short GRBs through a homogeneous analysis of a sample of more than 650 GRBs observed by *Swift*-X-Ray Telescope (XRT) (Burrows et al. 2005). We ask: What is the typical amount of energy released during the different X-ray LC phases? Does the X-ray emission retain any kind of ‘memory’ of the prompt  $\gamma$ -ray phase? GRBs are traditionally classified into long and short according to their prompt  $\gamma$ -ray properties: Do short GRBs show a distinct behaviour in the X-rays as well? Is it possible to find a *universal* (i.e. common to long and short GRBs) scaling that involves prompt and X-ray properties? This set of still open questions constitutes the major reason to undertake the present investigation.

Previous attempts mainly concentrated on *observer* frame properties and tried to understand to what extent the observations could be reconciled with the standard forward shock model (e.g. O’Brien et al. 2006; Butler 2007; Butler & Kocevski 2007; Liang, Zhang & Zhang 2007; Willingale et al. 2007; Liang et al. 2008; Evans et al. 2009; Racusin et al. 2009, 2011). This effort led to the identification of serious difficulties of the standard picture. We build on previous results and adopt here a different approach: instead of comparing observations with a particular physical model, we take advantage of the large sample size and look for *correlations* between the X-ray and  $\gamma$ -ray properties of GRBs *any* physical model will have to explain. We complement previous studies with the following.

- (i) Homogeneous analysis of GRBs in a *common rest-frame* energy band (0.3–30 keV).
- (ii) Statistics and properties of the temporal variability superimposed on the smooth X-ray decay.
- (iii) Comparative study of long versus short GRB X-ray afterglows.
- (iv) Study of the prompt  $\gamma$ -ray versus X-ray connection: notably, we report on the existence of a *universal* scaling involving prompt and X-ray parameters.

Hereafter, we will refer to the X-ray signal recorded by *Swift*-XRT after a GRB trigger as ‘X-ray LC’ and explicitly do not use the word ‘afterglow’ to avoid confusion (‘afterglow’ refers to the standard interpretation). Uncertainties are given at 68 per cent confidence level (c.l.) unless explicitly mentioned. Standard cosmological quantities

have been adopted:  $H_0 = 70 \text{ km s}^{-1} \text{ Mpc}^{-1}$ ,  $\Omega_\Lambda = 0.7$  and  $\Omega_M = 0.3$ . The results from our analysis are publicly available.<sup>1</sup>

## 2 DATA ANALYSIS

We select GRBs observed by *Swift*-XRT from the beginning of science operations in 2004 December through the end of 2010. The starting sample includes 658 GRBs; 36 belong to the class of short GRBs. Following Margutti et al. (2011b), the short or long nature of each event is established using the combined information from the duration, hardness and spectral lag of its prompt  $\gamma$ -ray emission: a prompt  $\gamma$ -ray duration  $T_{90} \lesssim 2$  s coupled to a hard  $\gamma$ -ray emission with photon index  $\Gamma \lesssim 1.5$  and a negligible spectral lag are considered indicative of a short GRB nature.

For each GRB, the data reduction comprises four steps:

- (i) extraction of count-rate LCs in the 0.3–10 keV energy band,
- (ii) time-resolved spectral analysis,
- (iii) flux calibration in the observer frame 0.3–10 keV energy band and luminosity calibration in the rest-frame 0.3–30 keV energy range for the sub-sample of GRBs with known redshift and
- (iv) LC fitting.

The *Swift*-XRT data have been analysed using the latest version of the *HEASOFT* package available at the time of the analysis (v. 6.10). For each GRB we started from calibrated event lists and sky images as distributed by the HEASARC archive.<sup>2</sup> The following analysis made extensive use of the *XRTDAS* software package. The additional automated processing was performed via custom *IDL* scripts. Details on the procedure followed can be found in Margutti (2009).<sup>3</sup> Here we note the following.

- (i) While agreeing on the major steps, the data extraction adopted here is slightly different from the methods presented in Evans et al. (2007, 2009); however, after comparing every single LC obtained with the two techniques, we find that the methods lead to consistent results.
- (ii) Our flux and luminosity LC calibration is based on a time-resolved spectral analysis which is able to capture the spectral evolution of the source with time. Uncertainties arising from the spectral analysis have also been propagated into the final flux and luminosity LCs (this is essential to compute the significance of positive temporal fluctuations superimposed on the smoothly decaying LC; see Section 2.1).
- (iii) The intrinsic neutral hydrogen absorbing column  $\text{NH}_{\text{HG}}$  of each GRB was computed extracting a spectrum in the widest interval of time with no apparent spectral evolution. The best-fitting  $\text{NH}_{\text{HG}}$  was used as a frozen parameter in the time-resolved spectral analysis above. The Galactic contribution was frozen to the value in the direction of the burst as computed by Kalberla et al. (2005).

Since we corrected for the Galactic and intrinsic absorption, the final results are *unabsorbed* 0.3–10 keV (observer frame) flux LCs. For the sub-sample of GRBs with known redshift, we furthermore extracted *unabsorbed* luminosity LCs in the 0.3–30 keV (rest-frame) energy band (extrapolating the best-fitting power-law spectrum). We conservatively use only  $z$  derived from optical spectroscopy and photometric redshifts for which potential sources of

<sup>1</sup> A demo version of the website is currently available at [http://www.grbtac.org/xrt\\_demo/GRB060312Afterglow.html](http://www.grbtac.org/xrt_demo/GRB060312Afterglow.html)

<sup>2</sup> <http://heasarc.gsfc.nasa.gov/cgi-bin/W3Browse/swift.pl>

<sup>3</sup> Retrievable from <http://hdl.handle.net/10281/7465>

degeneracy (e.g. dust extinction) can be ruled out with high confidence. The complete list of reshifts used is reported in Table B1 (175 GRBs in our sample have redshift).

## 2.1 LC fitting

The X-ray LCs of GRBs for  $t \gtrsim 60$  s consist of smoothly decaying power laws or broken power laws with X-ray flares superimposed. Here we concentrate on the underlying smooth component.

We considered only GRBs whose statistics were good enough to allow us to extract a spectrum to convert their count-rate LCs into flux LCs (total of 437 GRBs out of 658). We first fitted the entire sample of flux LCs in the 0.3–10 keV (observer frame) energy band. We then focused on the sub-sample of GRBs with redshift and performed a second fit using the LCs in the common 0.3–30 keV (rest frame).

Our semi-automatic fitting routine is based on the  $\chi^2$  statistic and closely follows the procedure outlined in Margutti et al. (2011a). We fit the following models. Defining

$$f(N_1, \alpha_1, t) \equiv N_1 t^{-\alpha_1} \quad (1)$$

(where  $N_1$  and  $\alpha_1$  are the normalization and the slope of the power law, respectively) and

$$g(N_2, \alpha_2, \alpha_3, t_b, s, t) \equiv N_2 \left( \left( \frac{t}{t_b} \right)^{-\frac{\alpha_2}{s}} + \left( \frac{t}{t_b} \right)^{-\frac{\alpha_3}{s}} \right) \quad (2)$$

(where  $N_2$  is the normalization,  $\alpha_2$  and  $\alpha_3$  are the slopes of the broken power law;  $t_b$  is the break time while  $s$  is the smoothing parameter), the fitting models can be written as follows:

(i) simple power law (model 0):

$$F = f(N_1, \alpha_1, t), \quad (3)$$

(ii) smoothed broken power law (models Ia and Ib for  $s < 0$  and  $s > 0$ , respectively):

$$F = g(N_1, \alpha_1, \alpha_2, t_{b1}, s_1, t), \quad (4)$$

(iii) smoothed broken power-law plus initial (model IIa) power-law decay:

$$F = f(N_1, \alpha_1, t) + g(N_2, \alpha_2, \alpha_3, t_{b2}, s_1, t) \quad (5)$$

or final (model IIb) power-law decay:

$$F = g(N_1, \alpha_1, \alpha_2, t_{b1}, s_1, t) + f(N_2, \alpha_3, t), \quad (6)$$

(iv) double smoothly joined broken power laws (model III):

$$F = g(N_1, \alpha_1, \alpha_2, t_{b1}, s_1, t) + g(N_2, \alpha_3, \alpha_4, t_{b3}, s_2, t). \quad (7)$$

The model number follows from the number of break times. For model IIa (IIb, III) the first (second) break time is defined as the time when the second (first) component outshines the first (second) component. Fig. 1 illustrates the different models, while Fig. 2 shows the result for GRB 060312 taken as an example: in this case, the semi-automatic procedure identified two episodes of emission in excess of the smooth decay (model IIa). The number of GRBs for each LC type is listed in Table 1. We refer to the LCs as ‘type’ 0, Ia, Ib, IIa, IIb and type III GRBs in the following.

The best-fitting parameters together with their uncertainties and associated covariance matrix were then used to derive the 0.3–10 keV (observer frame) fluence of the entire LC from the *Swift*-XRT repointing time to the end of the observation. No temporal extrapolation was applied at this stage. Note that the contribution

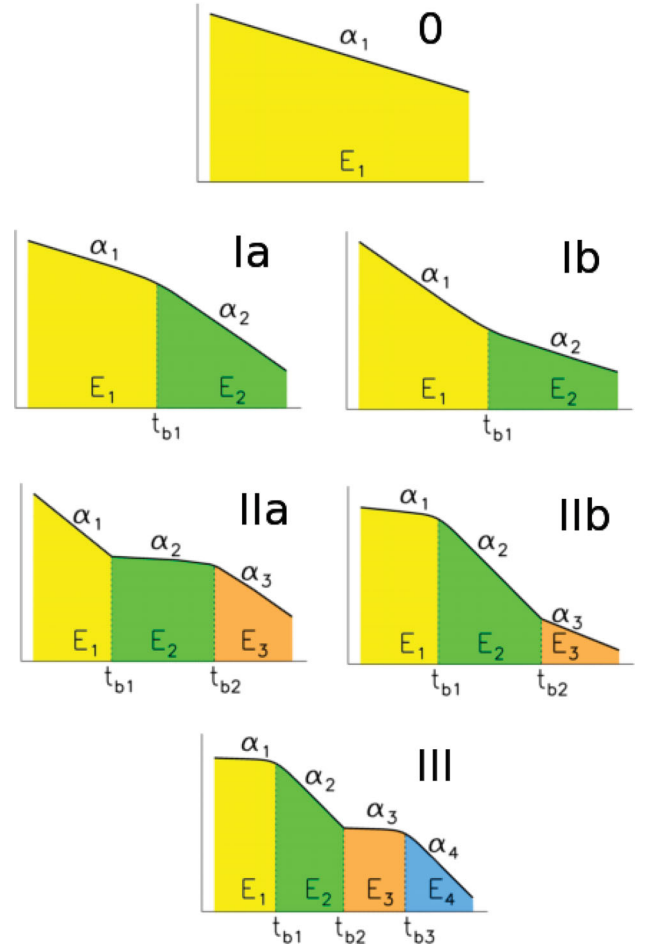


**Figure 1.** Sketch showing the different LC models used in this work. Both axes use logarithmic units.

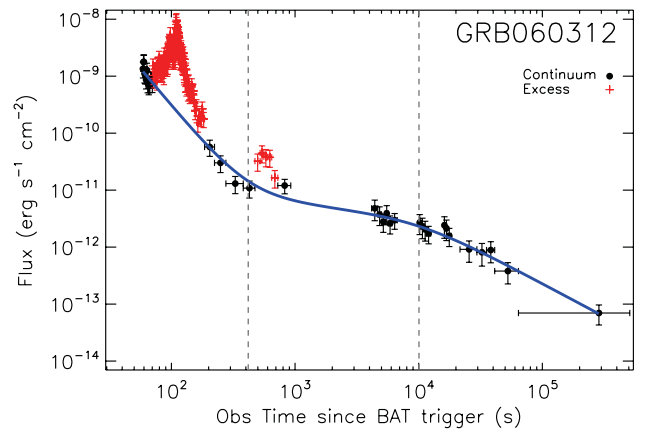


**Figure 2.** 0.3–10 keV unabsorbed flux LC of GRB 060312 with the best-fitting model superimposed (blue solid line). The red crosses mark the data points identified as ‘excesses’ during the semi-automatic fitting routine and subsequently removed from the fit to obtain the best-fitting power-law plus broken power-law model. Vertical dashed lines: best estimates of the break times obtained as described in the main text.

from significant positive fluctuations has *not* been included. The fluence of the different LC phases as defined by the temporal breaks was also calculated (Fig. 1). Results are listed in Tables B1 and B3. We then followed the very same procedure to fit the 0.3–30 keV

**Table 1.** Number of GRBs per LC type. For each type, the number of GRBs with complete LCs (C-GRBs, defined as promptly reprinted GRBs  $t_{\text{rep}} < 300$  s whose fading was followed up down to a factor of  $\sim 5$ –10 from the background limit) and with detected positive fluctuations (F-GRBs) with respect to the best-fitting smooth decay is also reported. GRBs are classified as either C- or U-like and either F- or N-like. U-like bursts have truncated LCs, while N-like GRBs show no evidence for flares. This classification refers to the 0.3–10 keV (observer frame) LCs.

	0	LC types				
		Ia	Ib	IIa	IIb	III
Total number of GRBs	114	89	61	133	18	22
C-GRBs	42	61	53	121	17	22
F-GRBs	23	16	24	48	8	10

(rest-frame) LCs. Table B5 reports the energetics in this energy range.

The list of LC points flagged as ‘excesses’ during the fitting procedure (e.g. red crosses of Fig. 2) constituted for each GRB the starting sample to look for significant positive fluctuations with respect to the best fit. The information contained in the covariance matrix was used to derive the uncertainties associated with the residuals with respect to the best fit (residuals were at this stage calculated on the *entire* LC). We first selected positive fluctuations with a minimum  $1\sigma$  significance. We furthermore require the positive fluctuations to show a rise plus decay *structure*: this procedure automatically excluded single data points scattering from the best fit. GRBs showing (not showing) such structures were flagged as ‘F’ (‘N’) in Tables B1–B5. GRB 060312 in Fig. 2, with two rising and decaying structures superimposed on the smooth decay, qualifies as ‘F’ event. The fluence (energy for known  $z$ ) of these excesses was calculated by simply integrating the flux of each LC bin over the bin duration (after subtracting the contribution from the underlying smoothly decaying emission). Errors were propagated accordingly and can be used to quantify how significant is the presence of emission in addition to the smooth power-law decay in each GRB. The fluence (energy) of positive fluctuations detected during the different LC phases (e.g. steep decay, plateau, normal decay, etc.) was also derived and listed in Tables B3 (0.3–10 keV, observer frame) and B5 (0.3–30 keV, rest frame). For simplicity, in the following we will use the word ‘flare’ to refer to statistically significant positive fluctuations detected on top of the smoothly decaying component, being however aware that different kinds of variability possibly contribute to the detected ‘flaring activity’.

### 3 LONG VERSUS SHORT GRB PROPERTIES

The analysis above reduces the X-ray LCs of GRBs to a set of measured parameters: temporal slopes; break times; total isotropic energy (fluence) and energy (fluence) associated with the different LC phases; flare energy (fluence); spectral photon index temporal evolution; intrinsic neutral hydrogen absorption. This constitutes an unprecedented set of information homogeneously obtained on the largest sample of GRBs to date and represents the natural sample to look for correlations among the parameters.

While we report the best-fitting parameters of the entire sample (Tables B1–B5), in the following we restrict our analysis to GRBs with ‘complete’ LCs, defined as those GRBs reprinted by XRT at  $t_{\text{rep}} < 300$  s and for which we were able to follow the fading of the XRT flux down to a factor of  $\sim 5$ –10 from the background limit (or, equivalently,  $t_{\text{end}} \gtrsim 4 \times 10^5$  s). These GRBs are flagged as ‘C’ in

**Table 2.** List of 19 short GRBs with complete LCs. GRBs with detected temporally extended emission are in boldface (Norris, Gehrels & Scargle 2011).

Short GRBs	
<b>050724</b>	051221A <b>051227</b> 060313 <b>061006</b>
061201	<b>070714B</b> 070724A 070809 <b>071227</b>
080123	<b>080503</b> 080919 090510 090515
090607	100117A 100816A 101219A

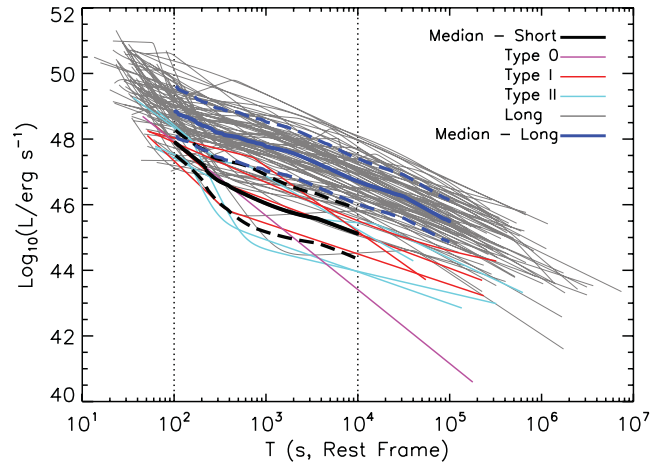


**Figure 3.** Best-fitting profiles of nine C-like short GRBs with the rest-frame time coverage  $10^2$ – $10^4$  s (colour lines) superimposed on the sample of long GRBs (grey lines). Black (blue) solid line: median  $\log(L)$  LC for short (long) GRBs; dashed lines: the  $1\sigma$  dispersion. The LCs have been calibrated in the rest-frame 0.3–30 keV energy band.

Tables B1–B5. The number of ‘C’-like GRBs per LC morphological type is reported in Table 1. ‘U’-like GRBs have instead truncated LCs. Short GRBs with complete LCs are listed in Table 2. Short GRBs with extended emission are in boldface (see Norris et al. 2011).

#### 3.1 Median X-ray LC of long and short GRBs

We select the sub-sample of C-like LCs of GRBs with redshift observed in the common rest-frame time intervals of  $10^2$ – $10^5$  s and  $10^2$ – $10^4$  s for long and short GRBs, respectively. These criteria resulted in a sample of 79 long GRBs and 9 short GRBs (Fig. 3). We consider here 0.3–30 keV (rest-frame) luminosity LCs.

We combined the best-fitting profiles of Section 2.1 to produce a median luminosity LC of a long GRB. The result is shown in Fig. 3: the median luminosity LC roughly decays as  $\sim t^{-1}$  [with a milder decay  $\sim t^{-0.9}$  for  $(0.5 < t < 4)$  ks and a steeper  $\sim t^{-1.2}$  decay after  $\sim 4$  ks]. With the possible exception of the shallower section, this is in rough agreement with the prediction of the standard afterglow theory<sup>4</sup> (Meszaros & Rees 1997; Sari et al. 1998).

The decay of the median LC is steeper for short GRBs ( $\propto t^{-1.3}$ ) than for long GRBs ( $\propto t^{-1}$ ) in the rest-frame time interval  $10^2$ – $10^4$  s; short GRB X-ray LCs are on average less luminous by a factor of  $\sim 10$ –30 than long GRBs X-ray LCs. This conclusion holds also

<sup>4</sup> A steepening to  $\sim 1.5$ –2 is predicted after the jet-break time if the outflow is collimated into a jet (Rhoads 1999; Sari 1999).



**Table 3.** Characteristic quantities describing the parameter distributions [number of elements ( $\#$ ), mean ( $m$ ), median ( $M$ ), standard deviation (SD), skewness (SK)] and best-fitting values from a Gaussian fit [mean ( $\mu$ ), standard deviation ( $\sigma$ ), normalization ( $N$ )]. Fluences ( $S$ ) are given in  $10^{-6}$  erg cm $^{-2}$ , energies ( $E$ ) in  $10^{50}$  erg, fluxes ( $F$ ) in  $10^{-6}$  erg s $^{-1}$  cm $^{-2}$ , luminosities ( $L$ ) in  $10^{48}$  erg s $^{-1}$ , times ( $t$ ) in s, hydrogen column densities (NH) in  $10^{22}$  cm $^{-2}$ . Note that logarithmic (linear) units have been used in the upper (lower) half of the table. We refer the reader to Appendix A1 for the exact definition of the parameters listed below. X-ray energies, luminosities and intrinsic times have been computed in the rest-frame 0.3–30 keV energy band. All the other X-ray quantities refer to the 0.3–10 (observer frame) band.

	#	$m$	$M$	SD	SK	$\mu$	$\sigma$	$N$
$\text{Log}(S_\gamma)$	386	0.17	0.18	0.61	-0.07	$0.17 \pm 0.05$	$0.60 \pm 0.04$	$105.1 \pm 7.7$
$\text{Log}(T_{90})$	334	1.58	1.73	0.65	-1.18	$1.67 \pm 0.07$	$0.62 \pm 0.06$	$93.9 \pm 9.4$
$\text{Log}(E_\gamma^{15-150})$	151	2.06	2.37	0.93	-1.12	$2.26 \pm 0.14$	$1.02 \pm 0.1$	$91.6 \pm 9.$
$\text{Log}(E_{\gamma,\text{iso}})$	78	2.88	3.01	0.91	-0.89	$3.01 \pm 0.14$	$0.85 \pm 0.12$	$38.9 \pm 5.7$
$\text{Log}(E_{\text{pk}})$	78	2.64	2.71	0.52	-0.76	$2.56 \pm 0.1$	$0.47 \pm 0.069$	$23.6 \pm 4.7$
$\text{Log}(L_{\text{pk,iso}})$	85	2.43	2.51	1.00	-1.90	$2.51 \pm 0.19$	$0.91 \pm 0.12$	$61.0 \pm 9.3$
$\text{Log}(T_{90}^{\text{RF}})$	138	1.18	1.33	0.59	-0.65	$1.26 \pm 0.11$	$0.67 \pm 0.09$	$53.8 \pm 7.4$
$\text{Log}(\text{NH}_{\text{HG}})$	161	21.6	21.8	1.21	-3.54	$21.9 \pm 0.1$	$0.62 \pm 0.09$	$42.5 \pm 7.3$
$\text{Log}(S_X)$	316	-0.38	-0.42	0.62	0.23	$-0.46 \pm 0.05$	$0.57 \pm 0.04$	$68.6 \pm 5.3$
$\text{Log}(S_X^{\text{FL}})$	115	-0.81	-0.76	0.82	-0.38	$-0.76 \pm 0.12$	$0.89 \pm 0.12$	$51.3 \pm 6.0$
$\text{Log}(S_{1,X})$	211	-0.90	-0.92	0.80	0.12	$-0.89 \pm 0.10$	$0.88 \pm 0.06$	$97.2 \pm 7.9$
$\text{Log}(S_{2,X})$	316	-0.58	-0.61	0.63	0.14	$-0.57 \pm 0.07$	$0.70 \pm 0.06$	$102.2 \pm 8.5$
$\text{Log}(S_{1,X}^{\text{FL}})$	62	-0.75	-0.69	0.73	-0.38	—	—	—
$\text{Log}(S_{2,X}^{\text{FL}})$	71	-1.08	-0.98	0.90	0.03	$-1.08 \pm 0.17$	$0.95 \pm 0.16$	$36.7 \pm 5.6$
$\text{Log}(E_{X,\text{iso}})$	126	1.67	1.84	0.81	-0.67	$1.82 \pm 0.08$	$0.88 \pm 0.08$	$31.1 \pm 2.5$
$\text{Log}(E_X^{\text{FL}})$	59	1.25	1.40	0.97	-0.64	—	—	—
$\text{Log}(E_{1,X})$	86	1.00	1.04	0.92	-0.28	$1.10 \pm 0.11$	$0.94 \pm 0.08$	$40.7 \pm 3.6$
$\text{Log}(E_{2,X})$	126	1.45	1.63	0.92	-0.94	$1.63 \pm 0.11$	$0.82 \pm 0.10$	$63.2 \pm 7.0$
$\text{Log}(E_{1,X}^{\text{FL}})$	35	1.13	1.38	1.00	-0.78	—	—	—
$\text{Log}(E_{2,X}^{\text{FL}})$	38	1.04	1.14	0.98	0.01	—	—	—
$\text{Log}(t_i)$	155	2.66	2.56	0.48	1.06	—	—	—
$\text{Log}(t_f)$	155	3.94	3.93	0.73	0.19	$3.93 \pm 0.14$	$0.8 \pm 0.12$	$59.2 \pm 8.9$
$\text{Log}(F_i)$	155	-4.23	-4.26	0.83	-0.14	$-4.18 \pm 0.11$	$0.89 \pm 0.12$	$61.1 \pm 6.6$
$\text{Log}(F_f)$	155	-5.01	-4.94	0.80	-0.12	$-4.99 \pm 0.11$	$0.80 \pm 0.08$	$63.4 \pm 6.9$
$\text{Log}(t_i^{\text{RF}})$	62	2.13	2.03	0.62	1.27	—	—	—
$\text{Log}(t_f^{\text{RF}})$	62	3.58	3.48	0.74	0.29	$3.53 \pm 0.11$	$0.75 \pm 0.09$	$23.0 \pm 2.9$
$\text{Log}(L_i)$	62	0.54	0.73	1.25	-1.07	$0.79 \pm 0.19$	$1.26 \pm 0.16$	$46.6 \pm 5.5$
$\text{Log}(L_f)$	62	-0.47	-0.19	1.19	-1.19	$0.04 \pm 0.33$	$1.41 \pm 0.29$	$38.2 \pm 6.8$
$\alpha_{\text{st}}$	213	3.96	3.56	2.34	3.95	$3.22 \pm 0.51$	$2.34 \pm 0.35$	$238.0 \pm 35.0$
$\alpha_{\text{sh}}$	155	-0.16	0.18	1.23	-4.06	$0.27 \pm 0.14$	$0.52 \pm 0.12$	$61.0 \pm 13.0$
$\alpha_{\text{n}}$	204	1.59	1.38	1.04	8.30	$1.34 \pm 0.13$	$0.49 \pm 0.11$	$93.0 \pm 19.0$

considering long GRBs in the *same* redshift bin. However, Fig. 3 clearly shows that the two samples slightly overlap (see also Gehrels et al. 2008). The steeper decay that characterizes short GRBs causes a progressive shift of their luminosity distribution towards the low end of the long GRB distribution.

### 3.2 Energetics of long and short GRBs

Table 3 reports the analysis of the parameter distributions derived from the LC fitting of Section 2. A complete list of symbols can be found in Appendix A1. The observed  $E_{X,\text{iso}}$  distribution peaks at  $\sim 7 \times 10^{51}$  erg, typically representing  $\sim 7$  per cent of the  $1\text{--}10^4$  keV (rest-frame)  $E_{\gamma,\text{iso}}$ . Fig. 4 shows that we are not sensitive to the population of bursts with  $E_{X,\text{iso}} < 10^{51}$  erg for  $z > 2$  (so that the

low-energy tail of the  $E_{X,\text{iso}}$  distribution is currently undersampled). This is likely a non-detectability zone, consequence of the  $E_{X,\text{iso}} \propto E_{\gamma,\text{iso}}^{0.8}$  of Section 4. For  $z > 1$  there is no evidence for an evolution of the upper bound of  $E_{X,\text{iso}}$  with redshift, which may suggest that  $\sim 10^{53}$  erg is a physical boundary to the  $E_{X,\text{iso}}$  distribution (the record holder is GRB 080721 with  $E_{X,\text{iso}} \sim 10^{53}$  erg). In this respect we note that maximum budget  $E_{\text{max}} \sim 10^{52}$  erg $^5$  is predicted by magnetar models (Usov 1992). The same pattern is followed by the flare energy  $E_X^{\text{FL}}$ : for  $z > 2$  we are not sensitive to  $E_X^{\text{FL}} < 10^{50}$  erg.

<sup>5</sup> It is not given that GRB 080721 violates this limit:  $E_{X,\text{iso}}$  represents the *isotropic* equivalent X-ray energy, an overestimate to the true value if the emission – as we believe – is beamed.

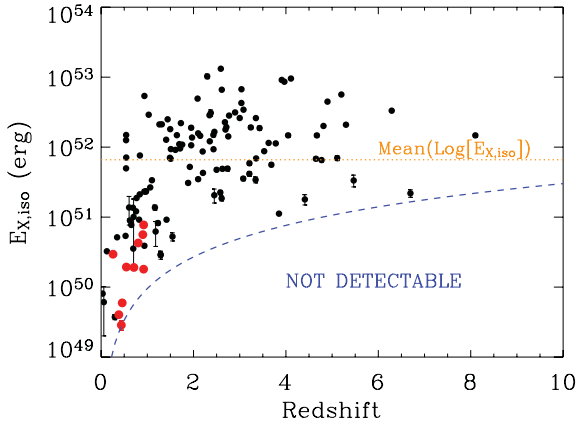


**Figure 4.** 0.3–30 keV (rest-frame) X-ray energy as a function of redshift. Black (red) points: long (short) GRBs. Blue dashed line: empirically derived detectability threshold. For  $z > 2$  we are not sensitive to GRBs with  $E_{X, \text{iso}} \lesssim 10^{51}$  erg. For  $z > 1$ , there is no evidence for an evolution of the upper bound of  $E_{X, \text{iso}}$  with redshift.

Observations suggest that the GRB X-ray LCs consist of two distinct phases (see e.g. Willingale et al. 2007): a first steep decay phase tightly connected to the prompt  $\gamma$ -ray emission (Tagliaferri et al. 2005; Goad et al. 2006) and a second phase characterized by a flattening of the LC (with limited evidence for spectral evolution; see e.g. Liang et al. 2007) followed by a ‘normal decay’ phase. Type IIa GRBs (Fig. 1) clearly show the presence of both components, with energy  $E_{1, X} = E_1$  and  $E_{2, X} = E_2 + E_3$ , respectively; for type Ia LCs, the lack of spectral evolution and the typically mild slope  $\alpha_1$  resembling  $\alpha_2$  of type IIa lead us to identify  $E_{2, X} = E_1 + E_2$ ; type Ib GRBs show strong spectral evolution during the first LC segment: this together with the transition to a milder decay at  $t_{b,1}$  leads us to define  $E_{1, X} = E_1$  and  $E_{2, X} = E_2$ ; in type IIb LCs the spectral and temporal properties of the first segment (with slope  $\alpha_1$ ) strongly suggest that *Swift*-XRT caught the end of the prompt emission in the X-rays: we therefore define  $E_{1, X} = E_1 + E_2$  and  $E_{2, X} = E_3$ ; the same is true for type III GRBs: in this case we define  $E_{1, X} = E_1 + E_2$  and  $E_{2, X} = E_3 + E_4$ . The two phases release comparable energy (see Table 3), with  $E_{1, X}$  and  $E_{2, X}$  peaking at  $\sim 1.1 \times 10^{51}$  and  $\sim 4 \times 10^{51}$  erg, respectively.

In each distribution, short GRBs populate the low-energy tail:  $E_{X, \text{iso}}^{\text{short}} \sim 10^{50}$  erg, which is approximately two orders of magnitude less than a typical long GRB. Fig. 4 also shows that short GRBs are less energetic than long GRBs in the *same* redshift bin. A systematic difference between the – still poorly constrained – jet opening angles of long and short GRBs, with short GRBs being less collimated than long GRBs, could in principle mitigate this energy gap. If we compare the energy released during the two phases separately (i.e. early steep decline versus plateau plus subsequent decay), we find an indication that short GRBs are more energetically deficient during the second phase than in the first phase, i.e.  $E_{X,2}^{\text{short}}/E_{X,2}^{\text{long}} \sim 0.014$  and  $E_{X,1}^{\text{short}}/E_{X,1}^{\text{long}} \sim 0.054$ . This argues against a beaming-related explanation, since the jet opening angles of long and short GRBs are expected to be more similar at late than at early times. Short GRB LCs decay faster than long GRBs in the X-rays, typically resulting in shorter observations ( $t_{\text{end}} \sim 10^4$  s versus  $t_{\text{end}} \sim 10^5$  rest frame); however, using the average  $L \propto t^{-1.3}$  scaling above, we find  $E_{X,2}^{\text{short}}(t < 10^4 \text{ s}) \sim E_{X,2}^{\text{short}}(t < 10^5 \text{ s})$ . Thus, the relatively lower measured energy of the later LC phase in short GRBs compared to long GRBs is not due to the shorter observations.

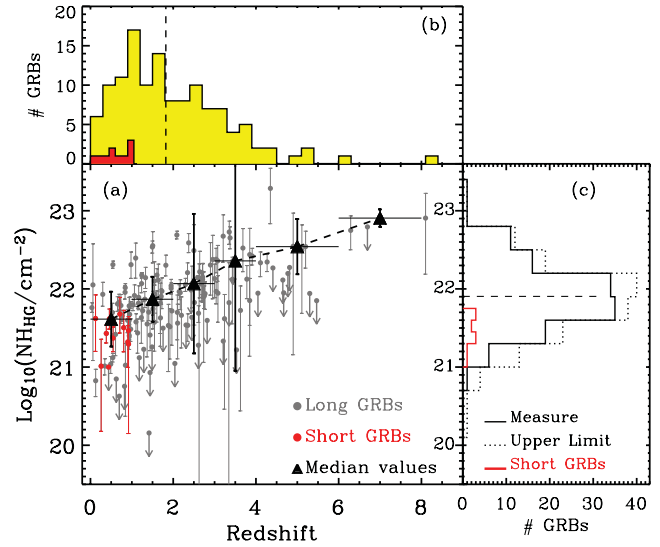


**Figure 5.** (a) Intrinsic neutral hydrogen absorption versus redshift for long and short GRBs (grey and red dots, respectively). 90 per cent upper limits are marked with arrows. Median  $\text{NH}_{\text{HG}}$  values in different redshift bins are indicated with filled triangles: for each bin, the error bars span the  $1\sigma$   $\text{NH}_{\text{HG}}$  dispersion. (b) Redshift distribution of the sample of long (yellow) and short (red) GRBs. (c) Intrinsic neutral hydrogen distribution for long (black line) and short (red line) GRBs. The dashed histogram includes upper limits. In panels (b) and (c) a dashed line indicates the median value for the entire distributions ( $\langle z \rangle = 1.82$ ,  $\langle \text{NH}_{\text{HG}} \rangle = 10^{21.8} \text{ cm}^{-2}$ ).

### 3.3 Intrinsic neutral hydrogen absorption in long and short GRBs

The distribution of the intrinsic neutral hydrogen columns  $\text{NH}_{\text{HG}}$  is portrayed in Fig. 5, panel (c). The distribution of *measured*  $\text{NH}_{\text{HG}}$  is found to have an average value<sup>6</sup> of  $m = 10^{21.6} \text{ cm}^{-2}$ . When modelled with a lognormal distribution, the best-fitting mean and standard deviation are,  $\mu = 21.9 \pm 0.1$  and  $\sigma = 0.6 \pm 0.1$ , in agreement with the estimates by Campana et al. (2010, 2012) obtained on smaller samples. However, different from Campana et al. (2010): (i) our sample contains a larger number of GRBs for which no evidence of intrinsic absorption was found (upper limits in Fig. 5); and (ii) we find evidence for a larger population of highly absorbed ( $\text{NH}_{\text{HG}} > 10^{22} \text{ cm}^{-2}$ ) GRBs at low redshift ( $z < 2$ ).

A trend for increasing  $\text{NH}_{\text{HG}}$  with redshift is apparent in Fig. 5 (panel a); however, our sensitivity to small amounts of intrinsic absorption decreases with increasing redshift due to the fixed XRT band-pass, which explains the higher percentage of upper limits in the 4- to 6-redshift interval and is at least partially responsible for the observed trend. The sample is furthermore redshift selected, which implies a bias against highly extinguished GRBs. The severity of this bias is possibly redshift dependent, with dependence which is difficult to quantify.

Short GRBs map the low end of the  $\text{NH}_{\text{HG}}$  distribution, with an average absorption  $\text{NH}_{\text{HG}}^{\text{short}} = 10^{21.4} \text{ cm}^{-2}$  (mean of the logarithm of  $\text{NH}_{\text{HG}}$ ). Their properties are however *consistent* with the intrinsic absorption of *long* GRBs in the same redshift bin. A KS test comparing the  $\text{NH}_{\text{HG}}$  distribution of long and short GRBs with  $0 < z < 1$  reveals that there is *no* evidence for long GRBs to show higher  $\text{NH}_{\text{HG}}$  when compared to short GRBs in the same redshift bin (KS probability of 34 per cent). A possibility is that we missed

<sup>6</sup> Solar abundances are used to determine the best-fitting  $\text{NH}_{\text{HG}}$ .

the population of long GRBs with even higher  $N_{\text{H,GRB}}$  at low  $z$  (see above). This would imply that GRBs with low optical extinction but high  $N_{\text{H,GRB}}$  are typical of the high-redshift Universe only (Watson & Jakobsson 2012). We conclude that using the available data, caution must therefore be taken to interpret the long GRB  $N_{\text{H,GRB}}$  distribution as a proof of their association with star formation (Campana et al. 2010) unless this association is meant to be extended to short GRBs as well.

#### 4 PARAMETER CORRELATIONS

Here we proceed to look for two-parameter correlations involving both X-ray and  $\gamma$ -ray properties. From a blind analysis we found 199 statistically significant correlations (out of 946). We focus on the physically interesting correlations. The significance of each correlation is estimated using the  $R$  index  $r$ , the Spearman rank  $\rho$  and the Kendall coefficient  $K$  (Table 4). Only correlations for

which the chance probability associated with at least one of the test statistics is  $<10^{-3}$  have been listed. As a general note:

- (i) no significant correlation is found to involve the rest-frame  $T_{90}$ , the intrinsic  $N_{\text{H,GRB}}$  or the LC temporal slopes;
- (ii) we rescaled the LC temporal breaks  $t_b$  by the  $T_{90}$ , adding new parameters to our list:  $y \equiv t_b/T_{90}$ . However, the use of rescaled properties did not improve any of our correlations and are therefore not included in the following discussion.

The correlation coefficients and the best-fitting power-law parameters of each correlation are listed in Table 4. Our best-fitting procedure accounts for the sample variance (D'Agostini 2005).

##### 4.0.1 The link between the X-ray and prompt $\gamma$ -ray energy

Fig. 6 (left-hand panel) shows that  $E_{\text{X, iso}}$  is directly linked to the isotropic energy released in  $\gamma$ -rays during the prompt emission

**Table 4.** From left to right:  $X$  and  $Y$  parameters to be correlated [the best-fitting law reads  $\text{Log}(Y) = q + m\text{Log}(X)$ ]; best-fitting parameters as obtained accounting for the sample variance (D'Agostini 2005): slope ( $m$ ), normalization ( $q$ ), intrinsic scatter ( $\sigma$ ); errors are given at 95 per cent c.l. The last six columns list the value of the Spearman rank  $\rho$ , Kendall coefficient  $K$  and  $R$  index  $r$  statistics and relative chance probability  $p$ . For each parameter couple, values reported in the first line refer to the entire sample, while in the second line we restrict our analysis to the long GRB class. X-ray fluences, fluxes and observer frame times are computed in the 0.3–10 keV (observer frame) energy band; luminosities, energies and rest-frame times are computed in the 0.3–30 keV (rest-frame) energy band.

$X$	$Y$	$m$	$q$	$\sigma$	$\rho$	$p(\rho)$	$K$	$p(K)$	$r$	$p(r)$
$E_{\text{X, iso}}$	$E_{\text{X}}^{\text{FL}}$	$1.07 \pm 0.03$	$-4.1 \pm 72.2$	$0.57 \pm 0.01$	0.70	$3 \times 10^{-10}$	0.52	$2 \times 10^{-9}$	0.79	$<10^{-10}$
		$1.10 \pm 0.07$	$-5.9 \pm 198$	$0.58 \pm 0.01$	0.61	$3 \times 10^{-7}$	0.45	$6 \times 10^{-7}$	0.70	$10^{-9}$
$E_{\text{X, iso}}$	$L_{\text{f}}$	$1.21 \pm 0.06$	$-15.6 \pm 169$	$0.85 \pm 0.01$	0.58	$6 \times 10^{-7}$	0.45	$2 \times 10^{-7}$	0.70	$3 \times 10^{-10}$
		$1.26 \pm 0.08$	$-18.1 \pm 206$	$0.85 \pm 0.01$	0.55	$3 \times 10^{-6}$	0.43	$8 \times 10^{-7}$	0.69	$10^{-9}$
$E_{\text{X, iso}}$	$L_{\text{i}}$	$1.39 \pm 0.06$	$-23.6 \pm 172$	$0.83 \pm 0.01$	0.63	$3 \times 10^{-8}$	0.49	$2 \times 10^{-8}$	0.75	$<10^{-10}$
		$1.37 \pm 0.08$	$-22.8 \pm 212$	$0.84 \pm 0.02$	0.60	$3 \times 10^{-7}$	0.46	$2 \times 10^{-7}$	0.72	$10^{-10}$
$t_{\text{f}}^{\text{RF}}$	$L_{\text{f}}$	$-1.23 \pm 0.03$	$51.9 \pm 0.46$	$0.77 \pm 0.01$	-0.80	$<10^{-10}$	-0.60	$<10^{-10}$	-0.77	$<10^{-10}$
		$-1.24 \pm 0.03$	$52.0 \pm 0.45$	$0.73 \pm 0.01$	-0.82	$<10^{-10}$	-0.62	$<10^{-10}$	-0.78	$<10^{-10}$
$L_{\text{f}}$	$E_{2, \text{X}}$	$0.52 \pm 0.01$	$26.8 \pm 11.8$	$0.47 \pm 0.00$	0.67	$2 \times 10^{-9}$	0.51	$5 \times 10^{-9}$	0.80	$<10^{-10}$
		$0.50 \pm 0.00$	$27.6 \pm 10.8$	$0.43 \pm 0.00$	0.65	$10^{-8}$	0.50	$2 \times 10^{-8}$	0.81	$<10^{-10}$
$E_{2, \text{X}}$	$E_{1, \text{X}}$	$0.42 \pm 0.02$	$29.1 \pm 43.2$	$0.81 \pm 0.01$	0.42	$4 \times 10^{-5}$	0.29	$4 \times 10^{-5}$	0.45	$6 \times 10^{-6}$
		—	—	—	0.28	$6 \times 10^{-3}$	0.19	0.06	0.29	$6 \times 10^{-3}$
$t_{\text{f}}$	$F_{\text{f}}$	$-0.79 \pm 0.01$	$-7.80 \pm 0.09$	$0.45 \pm 0.00$	-0.69	$<10^{-10}$	-0.50	$<10^{-10}$	-0.74	$<10^{-10}$
		$-0.79 \pm 0.01$	$-7.78 \pm 0.09$	$0.45 \pm 0.00$	-0.69	$<10^{-10}$	-0.50	$<10^{-10}$	-0.74	$<10^{-10}$
$E_{\gamma, \text{ iso}}$	$E_{\text{X, iso}}$	$0.79 \pm 0.01$	$10.0 \pm 20.6$	$0.39 \pm 0.00$	0.86	$<10^{-10}$	0.69	$<10^{-10}$	0.88	$<10^{-10}$
		$0.67 \pm 0.01$	$16.5 \pm 18.8$	$0.29 \pm 0.00$	0.82	$<10^{-10}$	0.63	$<10^{-10}$	0.88	$<10^{-10}$
$E_{\gamma, \text{ iso}}$	$E_{\text{X}}^{\text{FL}}$	$0.89 \pm 0.05$	$3.85 \pm 148$	$0.65 \pm 0.01$	0.64	$8 \times 10^{-5}$	0.48	$10^{-4}$	0.74	$3 \times 10^{-6}$
		$0.93 \pm 0.10$	$1.83 \pm 287$	$0.62 \pm 0.02$	0.56	$10^{-3}$	0.41	$10^{-3}$	0.67	$6 \times 10^{-5}$
$E_{\gamma, \text{ iso}}$	$E_{1, \text{X}}$	$0.67 \pm 0.03$	$15.9 \pm 91.3$	$0.81 \pm 0.02$	0.71	$2 \times 10^{-7}$	0.56	$2 \times 10^{-7}$	0.64	$5 \times 10^{-6}$
		$0.56 \pm 0.04$	$21.6 \pm 126$	$0.77 \pm 0.02$	0.62	$5 \times 10^{-5}$	0.48	$4 \times 10^{-5}$	0.54	$5 \times 10^{-4}$
$E_{\gamma, \text{ iso}}$	$E_{2, \text{X}}$	$0.92 \pm 0.01$	$2.96 \pm 33.5$	$0.51 \pm 0.01$	0.76	$<10^{-10}$	0.59	$<10^{-10}$	0.85	$<10^{-10}$
		$0.74 \pm 0.01$	$12.6 \pm 35.1$	$0.44 \pm 0.00$	0.67	$10^{-8}$	0.51	$2 \times 10^{-8}$	0.81	$<10^{-10}$
$E_{\gamma, \text{ iso}}$	$L_{\text{f}}$	$1.06 \pm 0.08$	$-8.86 \pm 227$	$1.03 \pm 0.04$	0.54	$9 \times 10^{-4}$	0.41	$7 \times 10^{-4}$	0.70	$8 \times 10^{-6}$
		$1.05 \pm 0.09$	$-8.43 \pm 260$	$1.06 \pm 0.04$	0.50	$3 \times 10^{-3}$	0.37	$3 \times 10^{-3}$	0.68	$2 \times 10^{-5}$
$E_{\text{pk}}$	$E_{\text{X, iso}}$	—	—	—	—	—	—	—	—	—
		$0.98 \pm 0.02$	$49.5 \pm 0.15$	$0.37 \pm 0.00$	0.63	$10^{-7}$	0.46	$5 \times 10^{-7}$	0.76	$<10^{-10}$
$L_{\text{pk}}$	$E_{\text{X, iso}}$	—	—	—	—	—	—	—	—	—
		$0.48 \pm 0.01$	$27.0 \pm 16.4$	$0.44 \pm 0.00$	0.58	$2 \times 10^{-7}$	0.42	$3 \times 10^{-7}$	0.74	$<10^{-10}$
$L_{\text{pk}}$	$L_{\text{f}}$	—	—	—	—	—	—	—	—	—
		$0.86 \pm 0.03$	$2.35 \pm 87.6$	$0.87 \pm 0.02$	0.50	$10^{-3}$	0.39	$5 \times 10^{-4}$	0.76	$7 \times 10^{-8}$
$L_{\text{pk}}$	$E_{2, \text{X}}$	—	—	—	—	—	—	—	—	—
		$0.60 \pm 0.01$	$20.3 \pm 15.9$	$0.43 \pm 0.00$	0.58	$10^{-7}$	0.42	$3 \times 10^{-7}$	0.82	$<10^{-10}$
$S_{\gamma}$	$S_{\text{X}}$	$0.77 \pm 0.01$	$-7.80 \pm 0.09$	$0.45 \pm 0.00$	0.79	$<10^{-10}$	0.59	$<10^{-10}$	0.77	$<10^{-10}$
		$0.82 \pm 0.00$	$-1.58 \pm 0.10$	$0.37 \pm 0.00$	0.78	$<10^{-10}$	0.58	$<10^{-10}$	0.78	$<10^{-10}$
$E_{\gamma, \text{ iso}}$	$L_{\text{X}}^{11\text{h}}$	$0.71 \pm 0.01$	$8.53 \pm 30.9$	$0.55 \pm 0.01$	0.66	$3 \times 10^{-10}$	0.49	$1 \times 10^{-9}$	0.77	$<10^{-10}$
		$0.54 \pm 0.01$	$17.5 \pm 29.6$	$0.45 \pm 0.00$	0.55	$2 \times 10^{-6}$	0.40	$2 \times 10^{-6}$	0.70	$<10^{-10}$
$E_{\gamma, \text{ iso}}$	$L_{\text{X}}^{10\text{min}}$	$0.93 \pm 0.01$	$-1.17 \pm 0.01$	$0.45 \pm 0.01$	0.87	$<10^{-10}$	0.67	$<10^{-10}$	0.88	$<10^{-10}$
		$0.78 \pm 0.01$	$6.73 \pm 32.6$	$0.40 \pm 0.00$	0.82	$<10^{-10}$	0.63	$<10^{-10}$	0.84	$<10^{-10}$

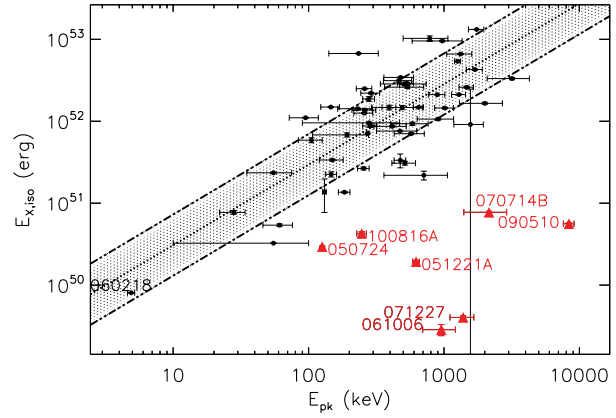
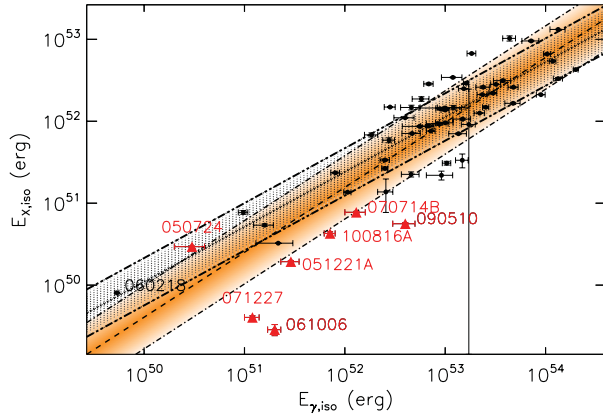


**Figure 6.** Correlations involving  $E_{\gamma, \text{iso}}$  ( $1\text{--}10^4$  keV, rest-frame),  $E_{X, \text{iso}}$  (0.3–30 keV, rest-frame) and the rest-frame prompt peak energy  $E_{\text{pk}}$ . Black dots (red triangles): long (short) GRBs. Dashed line: best-fitting power-law model for the entire short plus long GRBs sample. Dotted line: best-fitting model for the long GRB class only. The coloured and hatched areas mark the 68 per cent confidence region around the best fit. Short GRBs and outliers are named.

$E_{\gamma, \text{iso}}$ . A similar result was found by Willingale et al. (2007) on a smaller sample of GRBs. Here we show for the first time how short GRBs compare to long GRBs: notably, all short GRBs but GRB 050724 are outliers of the long GRB relation, with  $E_{X, \text{iso}}$  for short GRBs a factor of  $\sim 50$  below that for long GRBs and having a large dispersion (the  $E_{X, \text{iso}}$  distributions are almost distinct for long and short GRBs, as shown in Fig. 4). A clear exception is GRB 050724 (Barthelmy et al. 2005; Grupe et al. 2006) which had a bright and long-lived X-ray afterglow with a powerful late time rebrightening (Campana et al. 2006; Malesani et al. 2007; Bernardini et al. 2011). This difference may be understood in terms of a different radiative efficiency  $\eta_{\gamma}$  [where  $\eta_{\gamma} \equiv E_{\gamma}/(E_{\gamma} + E_K)$ ,  $E_K$  being the outflow kinetic energy] during the prompt emission between short GRBs and XRFs (X-ray flashes, i.e. GRBs with  $E_{\gamma, \text{iso}} \lesssim 10^{52}$  erg in Fig. 6): in this picture,  $\eta_{\gamma}^{\text{short}} > \eta_{\gamma}^{\text{XRF}}$ . The two populations are clearly distinct in terms of spectral peak energy during the prompt phase, with  $E_{\text{pk}}^{\text{short}} > E_{\text{pk}}^{\text{XRFs}}$  (Fig. 6). This may suggest that  $\eta_{\gamma}$  anticorrelates with  $E_{\text{pk}}$ : this is further investigated in Section 4.1.2.

Short and long GRBs occupy different areas of the  $E_{X, \text{iso}}$  versus  $E_{\text{pk}}$  plane (Fig. 6, upper-right panel) as well, demonstrating how the information from the X-ray LCs can be used to infer the GRB nature. Again, short GRBs fall below the long GRBs.

#### 4.0.2 The X-ray plateau and the prompt $\gamma$ -ray phase in long and short GRBs

In the literature, the shallow decay (or ‘plateau’) is associated with an LC phase generally characterized by a mild slope (and the absence of spectral evolution in the X-rays; Liang et al. 2007): this can be identified in type IIa and type III LCs. In type IIa (III) GRBs, this phase starts at  $t_i \equiv t_{b1}$  ( $t_i \equiv t_{b2}$ ) and ends at  $t_f \equiv t_{b2}$  ( $t_f \equiv t_{b3}$ ), with temporal slope  $\alpha_2$  ( $\alpha_3$ ) and energy  $E_2$  ( $E_3$ ). Short GRBs are underrepresented in the class of GRBs showing clear evidence of plateaus in the X-rays. Only two short GRBs (out of 19 with C-like LCs,<sup>7</sup> 10 per cent) possibly have plateaus: GRB 051221A ( $T_{90} = 1.4$  s) and GRB 070714B ( $T_{90} = 3$  s, extended emission not included). The corresponding percentage for long GRBs is instead  $\sim 37$  per cent.

<sup>7</sup> 36 was the number of short GRBs in our starting sample; only 19 of these have C-like LCs.

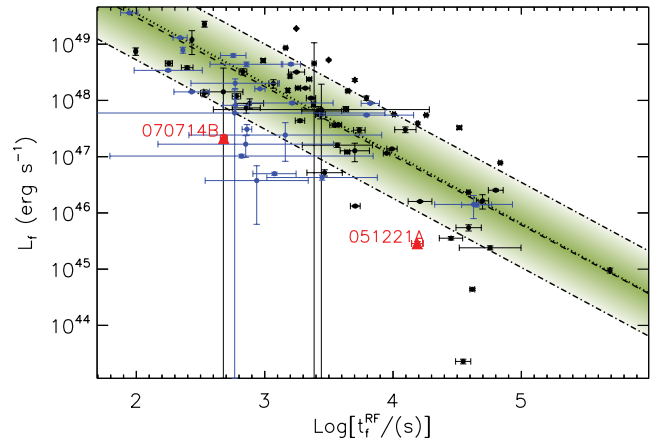


**Figure 7.** Luminosity at the end of the plateau phase, 0.3–30 keV (rest-frame), versus end time of the plateau. Colour coding is the same as in Fig. 6. Blue points denote type Ia LCs.

The luminosity at the end of the plateau phase  $L_f$  is directly related to the total energy released in the second LC phase  $E_{2, X}$  (Table 4):  $E_{2, X} \propto L_f^{0.52}$ . It is interesting to note that of the two short GRBs, 070714B is a clear outlier, while 051221A is only barely consistent with the correlation. The peculiar GRB 060218 also shows a lower than expected  $E_{2, X}$ . Dainotti, Cardone & Capozziello (2008) first reported a correlation between  $L_f$  and  $t_f^{\text{RF}}$  for long GRBs. Here we confirm the correlation (with best-fitting  $L_f \propto (t_f^{\text{RF}})^{-1.2}$ , Fig. 7) and show that the two short GRBs with clear evidence of plateau are *not* consistent with the same scaling.

#### 4.0.3 The link between the X-ray luminosity and the prompt $\gamma$ -ray energy release

The X-ray luminosity of the LC,  $L_X(t^{\text{RF}})$ , correlates with the  $\gamma$ -ray energy released during the prompt emission for *any*  $t^{\text{RF}}$  between 100 and  $10^5$  s. Here we arbitrarily select two rest-frame times (Fig. 8) as an example. We find that the scatter of the correlation evolves with time, with the  $L_X(t^{\text{RF}})$  versus  $E_{\gamma, \text{iso}}$  being tighter at early times (see Fig. 8). For this plot we require the GRBs to have been *observed* at these rest-frame times but relax the LC completeness requirement. No extrapolation of the observed LC is performed.



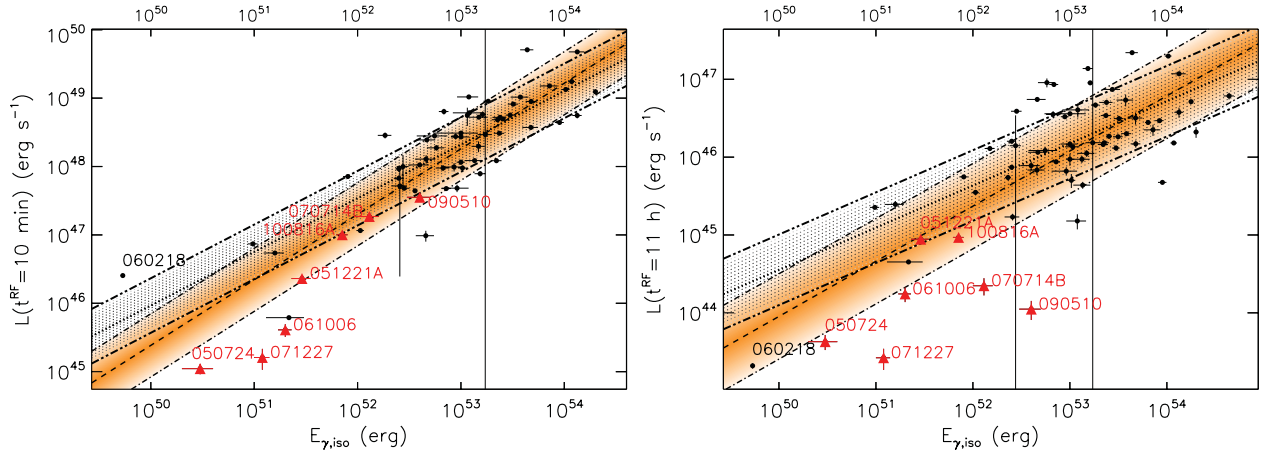


**Figure 8.** 0.3–30 keV (rest-frame) X-ray LC luminosity measured at 10 min (left-hand panel) and 11 h (right-hand panel) rest-frame versus  $E_{\gamma, \text{iso}}$ . Colour coding is the same as in Fig. 6. The scatter of the correlation increases with time.

At early times the LC luminosity tracks  $E_{\gamma, \text{iso}}$  with limited dispersion around the best-fitting model  $L_X^{10\text{min}} \propto E_{\gamma, \text{iso}}^{0.9}$ . Short GRBs tend to lie below the best-fitting law of the long GRB class. When compared to the same relation at much later times (11 h) we find that: (i) the relation is now more scattered, suggesting that the X-ray LCs are more directly linked to the prompt  $\gamma$ -ray phase at early than at late times; (ii) while the relation is highly scattered, we note that all short GRBs of our sample lie below the long GRB relation: this is consistent with the steeper decay of the average short GRB LCs when compared to the long GRB LCs found in Section 3.1. Our analysis therefore does not confirm the previous results from Nysewander, Fruchter & Pe’er (2009), who found that short and long GRBs are consistent with the *same*  $L_X$  versus  $E_{\gamma, \text{iso}}$  scaling (note however that their  $E_{\gamma, \text{iso}}$  is computed in a much narrower energy band).

#### 4.0.4 Observational biases: temporal extrapolation

The *Swift* repointing time  $t_{\text{rep}}$  and the end time of the observations  $t_{\text{end}}$  vary from GRB to GRB. Since  $E_{X, \text{iso}}$  is obtained by integrating the luminosity of each LC between  $t_{\text{rep}}$  and  $t_{\text{end}}$ , one may wonder what is the effect of using different integration times for different GRBs. This is quantified as follows. To estimate the amount of energy lost at the end of the observations, we extrapolated the best-fitting profile of each GRB up to  $10^7$  s (rest frame) and integrated the LC luminosity up until that time. Since GRBs may experience a jet break at late times (Racusin et al. 2009), this computation may lead to an overestimate of the real energy lost. The amount of energy possibly lost at the beginning of the observations<sup>8</sup> is estimated by conservatively extrapolating backwards in time the best-fitting profile to the minimum rest-frame *Swift* repointing time of our sample, which is 12.5 s. For GRBs with  $T_{90}^{\text{RF}} > 12.5$  s, we adopt  $T_{90}^{\text{RF}}$  as the starting time for the integration to avoid extrapolating the luminosity to unrealistic values. This approach leads to an *overestimate* of the amount of energy lost before  $t_{\text{rep}}$  for the large majority of GRBs, as can be seen comparing the extrapolated temporal profile we are adopting here to the *Swift*-Burst Alert Telescope (BAT) emission at the same rest-frame time (see e.g. the Swift Burst Analyser BAT

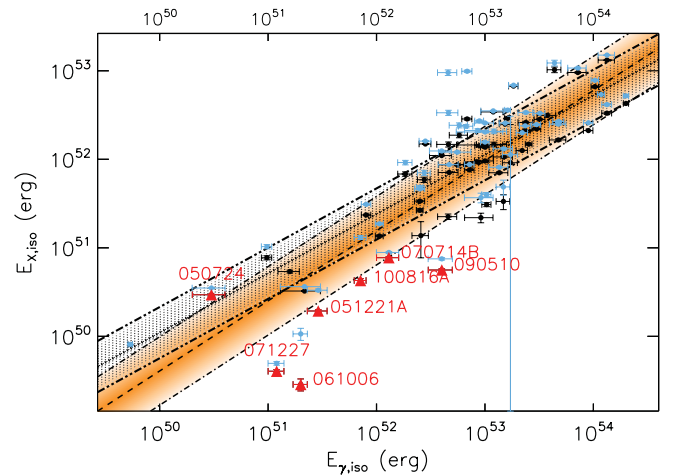


**Figure 9.** Impact of the temporal extrapolation of the observed LCs on the  $E_{X, \text{iso}}$  versus  $E_{\gamma, \text{iso}}$  correlation. Colour coding is the same as in Fig. 6. Light blue dots:  $E_{X, \text{iso}}$  values have been computed integrating the luminosity over a common rest-frame interval of time.

plus XRT LCs of GRB 050724; Evans et al. 2010). The corrected  $E_{X, \text{iso}}$  is shown in Fig. 9 (light blue points). Larger corrections (up to a factor of  $\sim 9$  for GRB 090510) are found to be applied to short GRBs. In spite of the very conservative approach, we find that short GRBs are still either barely compatible or not consistent with the long GRB relation (as before), while the long GRB relation is almost unaffected by this correction.

We therefore conclude that in a logarithmic space, the different rest-frame integration time used does not create or destroy correlations. The  $E_{X, \text{iso}}$  versus  $E_{\gamma, \text{iso}}$  correlation has been used here as an example: this result applies to all the relations presented in this paper.

### 4.1 MULTIPARAMETER CORRELATIONS

We look here for correlations involving more than two parameters (either from the X-rays or from the  $\gamma$ -rays). We first discuss the results from a principal component analysis (PCA; Section 4.1.1) and then show the existence of a tight three-parameter correlation directly linking  $E_{X, \text{iso}}$ ,  $E_{\gamma, \text{iso}}$  and  $E_{\text{pk}}$  both in long and short GRBs (Section 4.1.2).

<sup>8</sup> Note that the sample of C-like GRBs we use to look for correlations was pre-selected requiring an *observed* time of repointing  $t_{\text{obs}} < 300$  s to minimize this effect.

**Table 5.** The three most significant PCs (85 per cent of the total variance) projected upon  $\hat{E}_{\gamma, \text{iso}}$ ,  $\hat{E}_{\text{pk}}$ ,  $\hat{L}_{\text{pk}}$ ,  $\hat{T}_{90}^{\text{RF}}$  and  $\hat{E}_{\text{X, iso}}$ .

	PC1 40 per cent	PC2 66 per cent	PC3 85 per cent
$\hat{E}_{\gamma, \text{iso}}$	-0.561	0.141	0.171
$\hat{E}_{\text{pk}}$	-0.448	-0.300	-0.630
$\hat{L}_{\text{pk}}$	-0.502	-0.389	–
$\hat{T}_{90}^{\text{RF}}$	-0.121	0.794	-0.512
$\hat{E}_{\text{X, iso}}$	-0.466	0.331	0.588

#### 4.1.1 Principal component analysis

The PCA is a statistical technique designed to find patterns in data: it uses orthogonal transformations to convert a set of possibly correlated variables into linearly uncorrelated (orthogonal) variables. Given a set of  $N$  events (GRBs in our case) described by  $M$  parameters, the PCA consists of the diagonalization of the covariance matrix: the eigenvectors found are called principal components (PCs), while the eigenvalues consist of the variance associated with each PC (see Jolliffe 2002 for details). We performed a standardized PCA as recommended when the parameters have widely different variances: each parameter  $P$  is replaced by  $\hat{P} = (\text{Log}[P] - \overline{\text{Log}[P]}) / \sigma_{\text{Log}[P]}$ . In this case the matrix to be diagonalized is not a covariance, but a correlation matrix. Calculations were performed using the statistical package R.<sup>9</sup>

In Section 4 we showed that  $E_{\text{X, iso}}$  is the X-ray parameter that still keeps information from the prompt  $\gamma$ -ray energy release. We now investigate its relation to other prompt parameters, specifically  $E_{\text{pk}}$ ,  $L_{\text{pk}}$ ,  $T_{90}^{\text{RF}}$  (and  $E_{\gamma, \text{iso}}$ ), using the PCA. This set of parameters is measured simultaneously in 44 GRBs. Table 5 reports the three most significant PCs (86 per cent of the total variance) projected upon the original five variables. Each variable roughly contributes with comparable weight to the first PC; the second PC is instead dominated by  $\hat{T}_{90}^{\text{RF}}$ . The third PC relates  $\hat{E}_{\text{X, iso}}$  to  $\hat{E}_{\text{pk}}$ . This result suggests that while  $E_{\text{pk}}$ ,  $L_{\text{pk}}$ ,  $E_{\text{X, iso}}$  and  $E_{\gamma, \text{iso}}$  are in some way physically related to one another (see Section 4.1.2), the duration of the  $\gamma$ -ray energy release represents an *additional* degree of freedom to the system.

#### 4.1.2 A GRB universal scaling: $E_{\text{X, iso}}$ , $E_{\gamma, \text{iso}}$ and $E_{\text{pk}}$

We look for a three-parameter correlation involving  $E_{\text{X, iso}}$ ,  $E_{\gamma, \text{iso}}$  and  $E_{\text{pk}}$ . The three variables are found to be correlated (see Fig. 10) with the best-fitting law [obtained following the method by D’Agostini (2005)]

$$E_{\text{X, iso}} = 10^{(0.58 \pm 0.25)} \left[ \frac{E_{\gamma, \text{iso}}^{(1.00 \pm 0.06)}}{E_{\text{pk}}^{(0.60 \pm 0.10)}} \right], \quad (8)$$

where  $E_{\text{X, iso}}$ ,  $E_{\gamma, \text{iso}}$  and  $E_{\text{pk}}$  are in units of erg and keV, respectively. The intrinsic scatter is  $\sigma_{E_{\text{X, iso}}} = 0.30 \pm 0.03$  ( $1\sigma$ ). We note the following.

(i) This relation expands on the well-known  $E_{\text{pk}}-E_{\gamma, \text{iso}}$  (Amati et al. 2008 and references therein) relation with the introduction of a third parameter ( $E_{\text{X, iso}}$ ).

(ii) It combines information from the prompt *and* from the X-ray energy release which *follows* the prompt. While short GRBs are clear outliers of the  $E_{\text{pk}}-E_{\gamma, \text{iso}}$  relation, they perfectly fit into the

$E_{\text{X, iso}}-E_{\gamma, \text{iso}}-E_{\text{pk}}$  relation: the importance of the three-parameter relation is that it combines short and long GRBs on a common scaling. As a result, considering the *entire* short plus long GRB sample, the scatter is *reduced* by the introduction of the third variable (the intrinsic scatter of the Amati relation of our sample of long and short GRBs is  $\sigma_{E_{\text{pk}}} = 0.37$  as compared to the intrinsic scatter of the three-parameter relation on  $E_{\text{pk}}$  which is  $\sigma_{E_{\text{pk}}} = 0.29$ ). Restricting our analysis to long GRBs, we find  $\sigma_{E_{\text{pk}}} = 0.17$  both for the  $E_{\text{pk}}-E_{\gamma, \text{iso}}$  and for the three-parameter correlation.

(iii) Short GRBs (like GRB 051221A) and sub-energetic GRBs (like GRB 060218) occupy the *same* region of the  $E_{\text{pk}}-E_{\gamma, \text{iso}}-E_{\text{X, iso}}$  space. The same is true for the peculiar long GRB 060614, later reclassified as a possible short GRB (Gehrels et al. 2006). In general, GRBs seem to divide into two groups with ‘normal’ long GRBs occupying the upper-right area, and short and peculiar GRBs together with XRFs (e.g. 050416A, 060218, 081007, 060614 also have a spectral peak energy below 60 keV) share the same lower-left region of the plot.

(iv) The best-fitting slope of the  $E_{\text{X, iso}}$  versus  $E_{\gamma, \text{iso}}$  relation of Fig. 6 reads  $m = 0.79 \pm 0.01$  (see Table 4). The significant departure of  $m$  from 1 implies the more energetic long GRBs to have a *lower*  $\epsilon \equiv E_{\text{X, iso}}/E_{\gamma, \text{iso}} \propto 1/E_{\gamma, \text{iso}}^{0.2}$ , with short GRBs being outliers of this relation. Interestingly, equation (8) implies  $\epsilon \propto \frac{1}{E_{\text{pk}}^{0.60}}$ , suggesting that the key parameter determining the  $\gamma$ -ray to X-ray ratio is not  $E_{\gamma, \text{iso}}$  but the *spectral peak energy*  $E_{\text{pk}}$  irrespective of the nature of the GRB (either long or short). This is clear from the inset of Fig. 10: the higher the prompt peak energy the lower the  $\epsilon$  (the GRB with  $E_{\text{pk}} \sim 10^4$  keV is GRB 090510). We refer to Zhang et al. (2007) for a discussion of GRB radiative efficiencies derived from X-ray data.

(v) The  $\epsilon(E_{\text{pk}})$  scaling above can be interpreted as a *physical* dependence of the radiative efficiency  $\eta_{\gamma}$  on  $E_{\text{pk}}$ :  $\eta_{\gamma} \equiv E_{\gamma}/(E_{\gamma} + E_{\text{X}}) \approx E_{\gamma}/E_{\text{X}} \propto E_{\gamma}/E_{\text{X}}$  as long as  $E_{\gamma} < E_{\text{X}}$ . This would imply  $\eta_{\gamma} \propto E_{\text{pk}}^{0.6}$ . See Fan et al. (2012) for a discussion of this finding in the context of GRB photospheric models. Alternatively, a similar scaling could result for the long population if long GRBs with lower *isotropic*  $E_{\gamma, \text{iso}}$  are less beamed than high-energy GRBs during the prompt emission, but show otherwise similar beaming during the subsequent X-ray phase. In the first case, the  $\epsilon(E_{\text{pk}})$  scaling would give direct information about the dissipative processes behind GRBs; in the second case, it would be an observational effect that nevertheless would provide valuable information about GRB jets and their opening angles. A complete and detailed discussion is beyond the scope of this work and is provided by a companion paper (Bernardini et al. 2012).

(vi) In Section 4.0.4, we showed that the different time intervals over which  $E_{\text{X, iso}}$  has been estimated do not severely affect the  $E_{\text{X, iso}}-E_{\gamma, \text{iso}}-E_{\text{pk}}$ .

## 5 SUMMARY AND CONCLUSIONS

We performed a comprehensive statistical analysis of *Swift* X-ray LCs of 658 GRBs detected by XRT in the time period from the end of 2004 December to the end of 2010 December. For the first time (i) we present and analyse the properties of GRBs in a common rest-frame 0.3–30 keV energy band; (ii) we furthermore perform a comparative study of long and short GRBs; (iii) we cross-correlate the prompt  $\gamma$ -ray properties and the X-ray LC properties. We report below a summary of the major findings.

From the *spectral* analysis of GRBs with redshift (Section 3.3):

(1) We find evidence for high intrinsic neutral hydrogen absorption  $\text{NH}_{\text{HG}} \gtrsim 10^{22} \text{cm}^{-2}$  even at  $z \lesssim 2$ . The average value for long

<sup>9</sup> <http://www.r-project.org/>

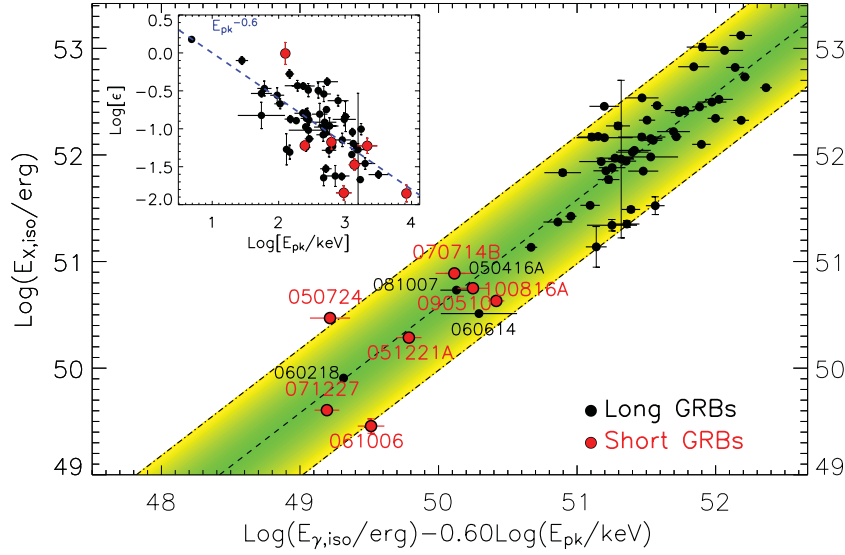


**Figure 10.** Three-parameter correlation involving  $E_{X, \text{iso}}$ ,  $E_{\gamma, \text{iso}}$  and  $E_{\text{pk}}$ . Dashed line: best-fitting relation (equation 8); dot-dashed lines: the 95 per cent confidence area around the best-fitting law. Notably, long and short GRBs share the same scaling, with short and sub-energetic GRBs (like GRB 060218) occupying the same area of the plot. Inset: evolution of the efficiency parameter  $\epsilon \equiv E_{X, \text{iso}}/E_{\gamma, \text{iso}}$  as a function of the spectral peak energy of the prompt emission  $E_{\text{pk}}$ . A reference  $\epsilon \propto E_{\text{pk}}^{-0.6}$  scaling has been marked with a blue dashed line.

GRBs is  $\text{NH}_{\text{HG}} \sim 10^{21.9} \text{ cm}^{-2}$  (mean value of the logarithm of the  $\text{NH}_{\text{HG}}$ ).

(2) Short GRBs map the low end of the distribution with mean  $\text{NH}_{\text{HG}} \sim 10^{21.4} \text{ cm}^{-2}$ . However, there is *no evidence* for short GRBs to show a lower  $\text{NH}_{\text{HG}}$  when compared to long GRBs in the *same* redshift bin.

The analysis of 297 *long* GRBs with complete X-ray LCs<sup>10</sup> reveals that:

(3) The average energy released in X-rays (0.3–30 keV, rest frame) is  $E_{X, \text{iso}} \sim 7 \times 10^{51} \text{ erg}$  typically representing  $\sim 7$  per cent of  $E_{\gamma, \text{iso}}$  (Section 3.2). The two quantities are statistically correlated:  $E_{X, \text{iso}} \propto E_{\gamma, \text{iso}}^{0.8}$ . Also,  $E_{X, \text{iso}} \propto E_{\text{pk}}$  (Section 4.0.1).

(4) The  $E_{X, \text{iso}}$  distribution does not extend beyond  $10^{53} \text{ erg}$  (Section 3.2) possibly suggesting the existence of a maximum available energy budget (the record holder is GRB 080721 with  $E_{X, \text{iso}} \sim 10^{53} \text{ erg}$ ). Also, for  $z > 2$  we are not sensitive to the population of GRBs with  $E_{X, \text{iso}} < 10^{51} \text{ erg}$ , so that the low-energy tail of the  $E_{X, \text{iso}}$  distribution is currently undersampled.

(5) The X-ray luminosity of the LCs at *any* rest-frame time between 100 and  $10^5 \text{ s}$  is found to correlate with  $E_{\gamma, \text{iso}}$  (Section 4.0.3): the scatter of this correlation increases with time which might suggest that early-time X-rays are more tightly related to the prompt phase.

In the case of *short* GRBs (19 have C-like LCs):

(6) The median luminosity LC of short GRBs (Section 3.1) is a factor of  $\sim 10$ – $30$  dimmer than long GRBs in the rest-frame time interval  $10^2$ – $10^4 \text{ s}$ , has a steeper average decay ( $\propto t^{-1.3}$  versus  $\propto t^{-1}$ ) and shows no evidence for clustering at late times (contrary to long GRBs).

(7) Short GRBs populate the low-energy tail of the  $E_{X, \text{iso}}$  distribution, with  $E_{X, \text{iso}}^{\text{short}} \sim \frac{1}{50} E_{X, \text{iso}}^{\text{long}}$  and an average  $E_{X, \text{iso}}^{\text{short}} \sim 10^{50} \text{ erg}$

(Section 3.2). Short GRBs are more energy deficient during the second LC phase when compared to long GRBs.

(8) Short bursts are clear outliers of the  $E_{X, \text{iso}}-E_{\gamma, \text{iso}}$  and  $E_{X, \text{iso}}-E_{\text{pk}}$  relations established by the long population, with  $E_{X, \text{iso}}^{\text{short}}$  a factor of  $\gtrsim 50$  below expectation (Section 4.0.1). Short GRBs are also found to lie below the  $L_X^{11\text{h}}$  versus  $E_{\gamma, \text{iso}}$  relation established by the long class.

(9) Short GRBs are underrepresented in the class of GRBs showing clear evidence of plateaus in the X-rays. Only 2 GRBs out of 19 possibly have plateaus (10 per cent). The corresponding percentage for long GRBs is instead  $\sim 37$  per cent. While the limited sample size does not allow us to draw firm conclusions, we note that X-ray plateaus are more commonly detected in *long* GRBs (Section 4.0.2).

(10) The two short GRBs with X-ray LC plateaus in our sample are outliers of the  $L_t$  versus  $t_t^{\text{RF}}$  relation (Section 4.0.2).

Irrespective of the long or short GRB nature, we find no statistically significant correlation involving the rest-frame prompt duration  $T_{90}^{\text{RF}}$ , the intrinsic column density  $\text{NH}_{\text{HG}}$  or the temporal slopes of the X-ray LCs (Section 4). The  $T_{90}^{\text{RF}}$  basically accounts for the second strongest PC (Section 4.1.1), suggesting that while  $E_{\text{pk}}$ ,  $L_{\text{pk}}$ ,  $E_{X, \text{iso}}$  and  $E_{\gamma, \text{iso}}$  are related to one another, the  $\gamma$ -ray duration represents an *additional* degree of freedom to the system.

We showed in Section 4.1.2 the existence of a three-parameter correlation that links  $E_{X, \text{iso}}$ ,  $E_{\gamma, \text{iso}}$  and  $E_{\text{pk}}$ :  $E_{X, \text{iso}} \propto (E_{\gamma, \text{iso}}^{1.00}/E_{\text{pk}}^{0.60})$ :

(i) Short and long GRBs share the *same* scaling.

(ii) This correlation implies  $\frac{E_{\gamma, \text{iso}}}{E_{X, \text{iso}}} \propto E_{\text{pk}}^{0.6}$  which can be interpreted as  $\eta_{\gamma} \propto E_{\text{pk}}^{0.6}$  (where  $\eta_{\gamma}$  is the radiative efficiency).

(iii) Standard long GRBs and short GRBs (together with peculiar GRBs and XRFs) occupy a different region of the  $E_{X, \text{iso}}-E_{\gamma, \text{iso}}-E_{\text{pk}}$  plane.

The results from our analysis are publicly available.<sup>11</sup>

<sup>10</sup> The total number of C-like GRBs is 316 (Table 1). 19 are short GRBs.

<sup>11</sup> A demo version of the website is currently available at [http://www.grbtac.org/xrt\\_demo/GRB060312Afterglow.html](http://www.grbtac.org/xrt_demo/GRB060312Afterglow.html)

## ACKNOWLEDGMENTS

RM thanks Lorenzo Amati and Lara Nava for sharing their data before publication. This research has made use of the XRT Data Analysis Software (XRTDAS) developed under the responsibility of the ASI Science Data Center (ASDC), Italy. MGB thanks ASI grant SWIFT I/004/11/0. PAE, KLP and JPO acknowledge financial support from the UK Space Agency. PR acknowledges financial contribution from the agreement ASI-INAF I/009/10/0.

## REFERENCES

- Amati L., Guidorzi C., Frontera F., Della Valle M., Finelli F., Landi R., Montanari E., 2008, *MNRAS*, 391, 577
- Barthelmy S. D. et al., 2005, *Nat*, 438, 994
- Bernardini M. G., Margutti R., Chincarini G., Guidorzi C., Mao J., 2011, *A&A*, 526, A27
- Bernardini M. G., Margutti R., Zaninoni E., Chincarini G., 2012, *MNRAS*, 425, 1199
- Burrows D. N. et al., 2005, *Space Sci. Rev.*, 120, 165
- Butler N. R., 2007, *ApJ*, 656, 1001
- Butler N. R., Kocevski D., 2007, *ApJ*, 663, 407
- Campana S. et al., 2006, *A&A*, 454, 113
- Campana S., Thöne C. C., de Ugarte Postigo A., Tagliaferri G., Moretti A., Covino S., 2010, *MNRAS*, 402, 2429
- Campana S. et al., 2012, *MNRAS*, 421, 1697
- Chincarini G. et al., 2007, *ApJ*, 671, 1903
- Chincarini G. et al., 2010, *MNRAS*, 406, 2113
- D'Agostini G., 2005, preprint (arXiv:e-prints)
- Dainotti M. G., Cardone V. F., Capozziello S., 2008, *MNRAS*, 391, L79
- Evans P. A. et al., 2007, *A&A*, 469, 379
- Evans P. A. et al., 2009, *MNRAS*, 397, 1177
- Evans P. A. et al., 2010, *A&A*, 519, A102
- Falcone A. D. et al., 2007, *ApJ*, 671, 1921
- Fan Y.-Z., Wei D.-M., Zhang F.-W., Zhang B.-B., 2012, *ApJ*, 755, L6
- Gehrels N. et al., 2004, *ApJ*, 611, 1005
- Gehrels N. et al., 2006, *Nat*, 444, 1044
- Gehrels N. et al., 2008, *ApJ*, 689, 1161
- Goad M. R. et al., 2006, *A&A*, 449, 89
- Grupe D., Burrows D. N., Patel S. K., Kouveliotou C., Zhang B., Mészáros P., Wijers R. A. M., Gehrels N., 2006, *ApJ*, 653, 462
- Grupe D. et al., 2007, *ApJ*, 662, 443
- Jolliffe I. T., 2002, *Principal Component Analysis*. Springer, Berlin
- Kalberla P. M. W., Burton W. B., Hartmann D., Arnal E. M., Bajaja E., Morras R., Pöppel W. G. L., 2005, *A&A*, 440, 775
- Kumar P., Narayan R., Johnson J. L., 2008, *MNRAS*, 388, 1729
- Liang E.-W., Zhang B.-B., Zhang B., 2007, *ApJ*, 670, 565
- Liang E.-W., Racusin J. L., Zhang B., Zhang B.-B., Burrows D. N., 2008, *ApJ*, 675, 528
- Lyons N., O'Brien P. T., Zhang B., Willingale R., Troja E., Starling R. L. C., 2010, *MNRAS*, 402, 705
- Malesani D. et al., 2007, *A&A*, 473, 77
- Margutti R., 2009, PhD thesis, Milano Bicocca University
- Margutti R., Bernardini G., Barniol Duran R., Guidorzi C., Shen R. F., Chincarini G., 2011a, *MNRAS*, 410, 1064
- Margutti R. et al., 2011b, *MNRAS*, 417, 2144
- Meszáros P., Rees M. J., 1997, *ApJ*, 476, 232
- Metzger B. D., Giannios D., Thompson T. A., Bucciantini N., Quataert E., 2011, *MNRAS*, 413, 2031
- Nava L., Ghirlanda G., Ghisellini G., Firmani C., 2008, *MNRAS*, 391, 639
- Norris J. P., Gehrels N., Scargle J. D., 2011, *ApJ*, 735, 23
- Nysewander M., Fruchter A. S., Pe'er A., 2009, *ApJ*, 701, 824
- O'Brien P. T. et al., 2006, *ApJ*, 647, 1213
- Paczynski B., 1986, *ApJ*, 308, L43
- Racusin J. L. et al., 2009, *ApJ*, 698, 43
- Racusin J. L. et al., 2011, *ApJ*, 738, 138
- Rhoads J. E., 1999, *ApJ*, 525, 737
- Sakamoto T. et al., 2011, *ApJS*, 195, 2
- Sari R., 1999, *ApJ*, 524, L43
- Sari R., Piran T., Narayan R., 1998, *ApJ*, 497, L17
- Tagliaferri G. et al., 2005, *Nat*, 436, 985
- Troja E. et al., 2007, *ApJ*, 665, 599
- Usov V. V., 1992, *Nat*, 357, 472
- Watson D., Jakobsson P., 2012, *ApJ*, 754, 89
- Willingale R. et al., 2007, *ApJ*, 662, 1093
- Woosley S. E., 1993, *ApJ*, 405, 273
- Zhang B. et al., 2007, *ApJ*, 655, 989

## APPENDIX A: GLOSSARY

This section provides the list of symbols used. As a general note, X-ray energies (fluences) were computed from the time of the *Swift*-XRT repointing up until the end of the observation; no temporal extrapolation was performed. The values reported assume isotropic emission. X-ray fluences and fluxes are reported in the 0.3–10 keV (observer frame) energy band; energies, luminosities and intrinsic time-scales are computed in the 0.3–30 keV (rest-frame) band.

(i)  $\alpha_n$ : temporal slope of the normal decay phase. Type Ia:  $\alpha_n = \alpha_2$ ; type IIa:  $\alpha_n = \alpha_3$ ; type III:  $\alpha_n = \alpha_4$ .

(ii)  $\alpha_{st}$ : temporal slope of the steep decay phase. Type Ib and IIa:  $\alpha_{st} = \alpha_1$ ; types IIb and III:  $\alpha_{st} = \alpha_2$  (see Fig. 1). The zero-time

**Table B1.** Best-fitting parameters of the 0.3–10 keV (observer frame) LCs in de-absorbed flux units, as obtained following the procedure outlined in Section 2.1: GRB name, LC type (as defined in Section 2.1), redshift, power-law indices ( $\alpha_1, \alpha_2, \alpha_3, \alpha_4$ ) and errors, break times ( $t_{b1}, t_{b2}, t_{b3}$ ) and errors, normalizations ( $N_1, N_2$ ) and errors, smoothing parameters ( $s_1, s_2$ ), prompt emission  $T_{90}$  [we refer to Sakamoto et al. (2011) for GRBs detected before 2009 December and to the refined BAT GCNs otherwise], power-law index of the first segment when  $t_0 = T_{90} (\alpha_1^{T_{90}})$  and error,  $\chi^2$ , degrees of freedom,  $p$  value. Normalizations are given in  $10^{-10} \text{ erg cm}^{-2} \text{ s}^{-1}$ , time in s. A redshift equal to 0 indicates that no reliable estimate of this parameter is available from the literature. For the other columns,  $-9$  indicates that the value is absent (i.e. there is no such LC phase). Note in the LC type column: C-GRBs (i.e. GRBs with complete LCs) are defined as promptly repointed GRBs  $t_{rep} < 300 \text{ s}$  whose fading was followed up to a factor of 5–10 from the background limit; if this is not the case, the GRB is flagged as U-like (i.e. GRB with truncated LC). The flag F (N) indicates that flares have (have not) been detected. This table is available in its entirety in a machine-readable form in the online journal. A portion is shown here for guidance.

GRB	Type	$z$	$\alpha_1$	$\sigma_{\alpha_1}$	$\alpha_2$	$\sigma_{\alpha_2}$	$\alpha_3$	$\sigma_{\alpha_3}$	$\alpha_4$	$\sigma_{\alpha_4}$	$\text{Log}[t_{b1}]$	$\sigma_{t_{b1}}$	$\text{Log}[t_{b2}]$	$\sigma_{t_{b2}}$	$\text{Log}[t_{b3}]$	$\sigma_{t_{b3}}$
041223	OUN	0	1.91	0.44	−9.0	−9.0	−9.0	−9.0	−9.0	−9.0	−9.0	−9.0	−9.0	−9.0	−9.0	−9.0
050124	OUN	0	1.44	0.17	−9.0	−9.0	−9.0	−9.0	−9.0	−9.0	−9.0	−9.0	−9.0	−9.0	−9.0	−9.0
050126	ICN	1.29	2.5	0.51	0.862	0.25	−9.0	−9.0	−9.0	−9.0	2.72	0.4	−9.0	−9.0	−9.0	−9.0
050128	IUN	0	0.758	0.12	1.38	0.14	−9.0	−9.0	−9.0	−9.0	3.69	0.38	−9.0	−9.0	−9.0	−9.0
050219A	ICN	0	3.68	0.36	0.779	0.11	−9.0	−9.0	−9.0	−9.0	2.4	0.054	−9.0	−9.0	−9.0	−9.0
050219B	OUN	0	1.42	0.044	−9.0	−9.0	−9.0	−9.0	−9.0	−9.0	−9.0	−9.0	−9.0	−9.0	−9.0	−9.0
050315	IICN	1.95	−0.295	0.18	0.819	0.037	3.83	0.18	−9.0	−9.0	2.71	0	3.82	0.14	−9.0	−9.0



Table B1 – continued

$N_1$	$\sigma_{N1}$	$N_2$	$\sigma_{N2}$	$s_1$	$s_2$	$T_{90}$	$\alpha_1^{T90}$	$\sigma_{\alpha T90}$	$\chi^2$	d.o.f.	p value
1.45e7	6.3e7	-9.0	-9.0	-9.0	-9.0	109.0	1.91	0.44	8.39	25.0	0.999
4.72e4	8e4	-9.0	-9.0	-9.0	-9.0	3.93	1.44	0.17	31.6	30.0	0.384
0.0673	0.11	-9.0	-9.0	0.5	-9.0	48.0	2.5	0.51	3.54	10.0	0.966
0.458	0.49	-9.0	-9.0	-0.5	-9.0	28.0	0.758	0.12	69.8	148.0	1.0
0.457	0.14	-9.0	-9.0	1.0	-9.0	23.8	3.13	0.31	56.6	79.0	0.973
1.26e5	4.8e4	-9.0	-9.0	-9.0	-9.0	28.7	1.42	0.044	81.9	127.0	0.999
0.179	0.027	2.15e9	1.8e9	-0.5	-9.0	95.6	-0.295	0.18	155.0	218.0	1.0

**Table B2.** 0.3–10 keV (observer frame) fluence table. From left to right: GRB name, LC type (as defined in Section 2.1), redshift, initial ( $T_{\min}$ ) and final ( $T_{\max}$ ) time of the observations, total fluence ( $S_{X,\text{iso}}$ ) with error, fluence of the different LC phases ( $S_1, S_2, S_3, S_4$ ) and errors, fluence of the flares in different parts of the LC ( $S_1^{\text{FL}}, S_2^{\text{FL}}, S_3^{\text{FL}}, S_4^{\text{FL}}$ ) and errors. Fluences are given in  $\text{erg cm}^{-2}$ . A redshift equal to 0 indicates that no reliable estimate of this parameter is available from the literature. A ‘-9’ indicates that the LC does not show such phase and the value of that parameter is therefore absent. Finally, for the columns containing information from flares superimposed on the power-law decay, 0 indicates that no statistically significant positive fluctuation has been detected. This table is available in its entirety in a machine-readable form in the online journal. A portion is shown here for guidance.

GRB	Type	$z$	$\text{Log}[T_{\min}]$	$\text{Log}[T_{\max}]$	$S_{X,\text{iso}}$	$\sigma_{SX}$	$S_1$	$\sigma_{S1}$	$S_2$	$\sigma_{S2}$	$S_3$	$\sigma_{S3}$	$S_4$	$\sigma_{S4}$
041223	OUN	0	4.22	4.45	$8.8\text{e}-8$	$6.7\text{e}-9$	-9.0	-9.0	-9.0	-9.0	-9.0	-9.0	-9.0	-9.0
050124	OUN	0	4.05	6.4	$1.6\text{e}-7$	$3.4\text{e}-8$	-9.0	-9.0	-9.0	-9.0	-9.0	-9.0	-9.0	-9.0
050126	ICN	1.29	2.12	4.83	$3.7\text{e}-8$	$6.8\text{e}-9$	$1.5\text{e}-8$	$2\text{e}-9$	$2.2\text{e}-8$	$6.3\text{e}-9$	-9.0	-9.0	-9.0	-9.0
050128	IUN	0	2.23	4.84	$7.9\text{e}-7$	$2.4\text{e}-8$	$4.6\text{e}-7$	$1.8\text{e}-8$	$3.3\text{e}-7$	$1.5\text{e}-8$	-9.0	-9.0	-9.0	-9.0
050219A	IUN	0	2.05	6.2	$3.5\text{e}-7$	$1.4\text{e}-7$	$4.1\text{e}-8$	$2\text{e}-9$	$3.1\text{e}-7$	$1.4\text{e}-7$	-9.0	-9.0	-9.0	-9.0
050219B	OUN	0	3.5	6.22	$9.4\text{e}-7$	$6.1\text{e}-8$	-9.0	-9.0	-9.0	-9.0	-9.0	-9.0	-9.0	-9.0
050315	IICN	1.95	1.92	5.93	$1.1\text{e}-6$	$3.3\text{e}-8$	$2.4\text{e}-7$	$1.4\text{e}-8$	$7\text{e}-8$	$8.8\text{e}-9$	$8\text{e}-7$	$2.8\text{e}-8$	-9.0	-9.0

Table B2 – continued

$S_1^{\text{FL}}$	$\sigma_{S1^{\text{FL}}}$	$S_2^{\text{FL}}$	$\sigma_{S2^{\text{FL}}}$	$S_3^{\text{FL}}$	$\sigma_{S3^{\text{FL}}}$	$S_4^{\text{FL}}$	$\sigma_{S4^{\text{FL}}}$
0	0	-9.0	-9.0	-9.0	-9.0	-9.0	-9.0
0	0	-9.0	-9.0	-9.0	-9.0	-9.0	-9.0
0	0	0	0	-9.0	-9.0	-9.0	-9.0
0	0	0	0	-9.0	-9.0	-9.0	-9.0
0	0	0	0	-9.0	-9.0	-9.0	-9.0
0	0	-9.0	-9.0	-9.0	-9.0	-9.0	-9.0
0	0	0	0	0	0	-9.0	-9.0

of the power-law decay is assumed to be the BAT trigger time (i.e.  $t_0 = 0$ ).

(iii)  $\alpha_{\text{st}}^{T90}$ : temporal slope of the steep decay phase assuming  $t_0 = T_{90}$ .

(iv)  $\alpha_{\text{sh}}$ : temporal slope of the shallow decay (or plateau) phase. This corresponds to  $\alpha_2$  and  $\alpha_3$  for type IIa and type III LCs, respectively.

(v)  $\Gamma_X$ : XRT 0.3–10 keV (observer frame) spectral photon index from this paper.

(vi)  $E_{\gamma, \text{iso}}$ : isotropic equivalent energy released during the prompt emission in the rest-frame 1–10<sup>4</sup> keV energy band from Amati et al. (2008).

(vii)  $E_{\text{pk}}$ : rest-frame peak energy of the  $\nu F_\nu$  spectrum during the prompt  $\gamma$ -ray emission from Amati et al. (2008).

(viii)  $F_t$  ( $L_t$ ): flux (luminosity) at the end of the plateau (i.e. at  $t = t_f$ ).

(ix)  $F_i$  ( $L_i$ ): flux (luminosity) at the beginning of the plateau (i.e. at  $t = t_i$ ).

(x)  $L_{\text{pk, iso}}$ : 1–10<sup>4</sup> keV (rest-frame) isotropic peak luminosity during the prompt emission from Nava et al. (2008).

(xi)  $L_X^{11\text{h}}$ : luminosity at 11 h rest frame.

(xii)  $L_X^{10\text{min}}$ : luminosity at 10 min rest frame.

(xiii)  $\text{NH}_{\text{tot}}$ : total neutral hydrogen column density.

(xiv)  $\text{NH}_{\text{HG}}$ : intrinsic neutral hydrogen column density at the redshift of the GRB.

(xv)  $S_{1,X}$  ( $E_{1,X}$ ): fluence (energy) released during the first phase of the X-ray LC. Types Ib and IIa:  $E_{1,X} = E_1$ ; types IIb and III:  $E_{1,X} = E_1 + E_2$ . Fluences follow the same definition scheme.  $E_1$ ,  $E_2$ ,  $E_3$  and  $E_4$  have been defined following Fig. 1.

(xvi)  $S_{2,X}$  ( $E_{2,X}$ ): fluence (energy) released during the second phase of the X-ray LC. Type Ia:  $E_{2,X} = E_1 + E_2$ ; type Ib:  $E_{2,X} = E_2$ ; type IIa:  $E_{2,X} = E_2 + E_3$ ; type IIb:  $E_{2,X} = E_3$ ; type III:  $E_{2,X} = E_2 + E_4$  (see Fig. 1). The definition scheme is the same for fluences.

(xvii)  $S_\gamma$  ( $E_\gamma^{15-150}$ ): 15–150 keV (observer frame) fluence (energy) released during the prompt emission as calculated by Sakamoto et al. (2011).

(xviii)  $S_X$  ( $E_{X, \text{iso}}$ ): X-ray fluence (energy).

(xix)  $S_X^{\text{FL}}$  ( $E_X^{\text{FL}}$ ): X-ray fluence (energy) associated with flares. For each GRB, the total fluence (energy) released in X-rays reads  $S_X^{\text{FL}} + S_X$  ( $E_X^{\text{FL}} + E_{X, \text{iso}}$ ).

(xx)  $S_{1,X}^{\text{FL}}$ ,  $S_{2,X}^{\text{FL}}$  ( $E_{1,X}^{\text{FL}}$ ,  $E_{2,X}^{\text{FL}}$ ): X-ray fluence (energy) of flares superimposed on the first and second LC phase.

(xxi)  $t_f$ ,  $t_f^{\text{RF}}$ ,  $t_f^{T90}$ : end time of the plateau phase: observer frame, rest frame and in  $T_{90}$  units. This parameter corresponds to  $t_{b2}$  and  $t_{b3}$  for type IIa and type III LC, respectively.

(xxii)  $t_i$ ,  $t_i^{\text{RF}}$ ,  $t_i^{T90}$ : start time of the plateau phase: observer frame, rest frame and in  $T_{90}$  units. This parameter corresponds to  $t_{b1}$  and  $t_{b2}$  for type IIa and type III LC, respectively.

(xxiii)  $\Delta t$ : plateau duration defined as  $t_f - t_i$ .

(xxiv)  $T_{90}$ ,  $T_{90}^{\text{RF}}$ : duration of the 15–150 keV prompt emission from Sakamoto et al. (2011) in the observer frame and in the rest frame, respectively.

## APPENDIX B: TABLES

**Table B2.** 0.3–10 keV (observer-frame) fluence table.

**Table B3.** 0.3–30 keV (rest-frame) energy table.

**Table B3.** 0.3–30 keV (rest-frame) energy table. From left to right: GRB name, LC type (as defined in Section 2.1), redshift, initial ( $T_{\min}$ ) and final ( $T_{\max}$ ) time of the observations, total energy ( $E_{X,\text{iso}}$ ) with error, energy of the different LC phases ( $E_1, E_2, E_3, E_4$ ) and errors, energy of the flares in different parts of the LC ( $E_1^{\text{FL}}, E_2^{\text{FL}}, E_3^{\text{FL}}, E_4^{\text{FL}}$ ) and errors. Energies are given in erg. A redshift equal to 0 indicates that no reliable estimate of this parameter is available from the literature. A ‘–9’ indicates that the LC does not show such phase and the value of that parameter is therefore absent. Finally, for the columns containing information from flares superimposed on the power-law decay, 0 indicates that no statistically significant positive fluctuation has been detected. This table is available in its entirety in a machine-readable form in the online journal. A portion is shown here for guidance regarding its form and content.

GRB	Type	$z$	$\text{Log}[T_{\min}]$	$\text{Log}[T_{\max}]$	$E_{X,\text{iso}}$	$\sigma_{E_X}$	$E_1$	$\sigma_{E1}$	$E_2$	$\sigma_{E2}$	$E_3$	$\sigma_{E3}$	$E_4$	$\sigma_{E4}$
050126	ICN	1.29	2.12	4.83	$3.7\text{e}-8$	$6.8\text{e}-9$	$1.5\text{e}-8$	$2\text{e}-9$	$2.2\text{e}-8$	$6.3\text{e}-9$	–9.0	–9.0	–9.0	–9.0
050315	IICN	1.95	1.92	5.93	$1.1\text{e}-6$	$3.3\text{e}-8$	$2.4\text{e}-7$	$1.4\text{e}-8$	$7\text{e}-8$	$8.8\text{e}-9$	$8\text{e}-7$	$2.8\text{e}-8$	–9.0	–9.0
050318	OUN	1.44	3.52	5.65	$2.5\text{e}-7$	$1.1\text{e}-8$	–9.0	–9.0	–9.0	–9.0	–9.0	–9.0	–9.0	–9.0
050319	IICN	3.24	1.98	6.15	$5\text{e}-7$	$5\text{e}-8$	$2.5\text{e}-8$	$3.6\text{e}-9$	$1.7\text{e}-7$	$6.7\text{e}-9$	$3\text{e}-7$	$4.9\text{e}-8$	–9.0	–9.0
050401	ICF	2.9	2.14	5.9	$1.2\text{e}-6$	$6.2\text{e}-8$	$5\text{e}-7$	$7.5\text{e}-9$	$7.3\text{e}-7$	$6.1\text{e}-8$	–9.0	–9.0	–9.0	–9.0
050408	OUN	1.24	3.41	6.47	$5.4\text{e}-7$	$3.9\text{e}-8$	–9.0	–9.0	–9.0	–9.0	–9.0	–9.0	–9.0	–9.0

**Table B3** – *continued*

$E_1^{\text{FL}}$	$\sigma_{E1^{\text{FL}}}$	$E_2^{\text{FL}}$	$\sigma_{E2^{\text{FL}}}$	$E_3^{\text{FL}}$	$\sigma_{E3^{\text{FL}}}$	$E_4^{\text{FL}}$	$\sigma_{E4^{\text{FL}}}$
0	0	0	0	–9.0	–9.0	–9.0	–9.0
0	0	0	0	0	0	–9.0	–9.0
0	0	–9.0	–9.0	–9.0	–9.0	–9.0	–9.0
0	0	0	0	0	0	–9.0	–9.0
0	0	0	0	–9.0	–9.0	–9.0	–9.0
0	0	–9.0	–9.0	–9.0	–9.0	–9.0	–9.0

## SUPPORTING INFORMATION

Additional Supporting Information may be found in the online version of this paper.

**Table B1.** Best-fitting parameters of the 0.3–10 keV (observer frame) light curves in de-absorbed flux units. (<http://mnras.oxfordjournals.org/lookup/suppl/doi:10.1093/mnras/sts066/-/DC1>).

Please note: Oxford University Press are not responsible for the content or functionality of any supporting materials supplied by the authors. Any queries (other than missing material) should be directed to the corresponding author for the article.

This paper has been typeset from a  $\text{\LaTeX}$  file prepared by the author.